

Generative Reduced Basis Method

Ngoc Cuong Nguyen^a

^a*Center for Computational Engineering, Department of Aeronautics and Astronautics,
Massachusetts Institute of Technology, 77 Massachusetts
Avenue, Cambridge, MA, 02139, USA*

Abstract

We present a generative reduced basis (RB) approach to construct reduced order models for parametrized partial differential equations. Central to this approach is the construction of generative RB spaces that provide rapidly convergent approximations of the solution manifold. We introduce a generative snapshot method to generate significantly larger sets of snapshots from a small initial set of solution snapshots. This method leverages multivariate nonlinear transformations to enrich the RB spaces, allowing for a more accurate approximation of the solution manifold than commonly used techniques such as proper orthogonal decomposition and greedy sampling. The key components of our approach include (i) a Galerkin projection of the full order model onto the generative RB space to form the reduced order model; (ii) *a posteriori* error estimates to certify the accuracy of the reduced order model; and (iii) an offline-online decomposition to separate the computationally intensive model construction, performed once during the offline stage, from the real-time model evaluations performed many times during the online stage. The error estimates allow us to efficiently explore the parameter space and select parameter points that maximize the accuracy of the reduced order model. Through numerical experiments, we demonstrate that the generative RB method not only improves the accuracy of the reduced order model but also provides tight error estimates.

Keywords: generative reduced basis method, generative snapshot method, finite elements, parametrized PDEs, reduced order modeling, model reduction

1. Introduction

Reduced basis (RB) methods are widely used for solving parametrized partial differential equations (PDEs) [1, 2, 3, 4, 5, 6, 7, 8, 9, 10, 11, 12, 13, 14, 15, 16, 17, 18, 19, 20, 21, 22]. One of the fundamental concepts underlying the effectiveness of RB methods is the Kolmogorov n -width, which measures how well a function space can be approximated by an n -dimensional subspace. The Kolmogorov n -width quantifies the smallest possible error when approximating the solution manifold of a parametrized PDE with an n -dimensional subspace [23]. It offers a theoretical framework for understanding the potential efficiency of a reduced basis: the lower the n -width for a given n , the more effectively the reduced basis can approximate the solution manifold.

The Kolmogorov n -width theory is related to Proper Orthogonal Decomposition (POD) [24, 25, 26]. POD provides a practical method for constructing low-dimensional approximation spaces by extracting the most energetic modes from a set of solution snapshots. For problems with smooth solution manifolds, where the Kolmogorov n -width decays rapidly, POD offers an effective low-dimensional approximation. However, POD faces limitations when the solution manifold contains localized, non-smooth, highly oscillatory features. In such cases, POD requires a large number of snapshots to achieve acceptable accuracy because the n -width decays slowly.

Greedy algorithms have been introduced to address some of the limitations of POD [27, 28, 29, 30, 31, 32, 33, 34, 35, 36]. The greedy algorithm, combined with a posteriori error estimates, provides an efficient way to explore the parameter space and select the most informative parameter points. Both POD and the greedy algorithm encounter difficulties when applied to problems with slowly decaying Kolmogorov n -width or high-dimensional parameter spaces. In such cases, the solution manifold may not be adequately captured by a small set of snapshots, limiting the accuracy of these methods.

To improve the accuracy and efficiency of ROMs, several extensions to traditional RB methods have been proposed. Adaptive RB approach partitions the parameter domain and constructs an individualized ROM for each partition [4, 37, 38, 39]. Other adaptive RB techniques have been developed to update the RB space during the online phase according to various criteria associated with changes of the system dynamics in parameters and time [40, 41, 42, 43, 44]. Multiscale RB method [45, 46] and static condensation RB element method [47, 8, 48] have been developed to handle problems in which the coefficients of the differential operators are characterized by a

large number of independent parameters. Boyaval et al. [49, 50] develop a RB approach for solving variational problems with stochastic parameters and reducing the variance in the Monte-Carlo simulation of a stochastic differential equation [21, 51].

RB methods applied to convection-dominated problems often struggle due to slowly decaying Kolmogorov n widths caused by moving shocks and discontinuities. To address this issue, various techniques recast the problem in a more suitable coordinate frame using parameter-dependent maps. Approaches include POD-Galerkin methods with shifted reference frames [52], optimal transport methods [53, 54, 55, 56, 57], and phase decomposition. Recent methods like shifted POD [58], transport reversal [59], and transport snapshot [60] use time-dependent shifts, while registration [61] and shock-fitting methods [62, 63] minimize residuals to determine the map for better low-dimensional representations.

Model reduction on nonlinear manifolds was originated with the work [64] on reduced-order modeling of nonlinear structural dynamics using quadratic manifolds. This approach was further extended through the use of deep convolutional autoencoders by Lee and Carlberg [65]. Recently, quadratic manifolds are further developed to address the challenges posed by the Kolmogorov barrier in model order reduction [66, 67]. Another approach is model reduction through lifting or variable transformations, as demonstrated by Kramer and Willcox [68], where nonlinear systems are reformulated in a quadratic framework, making the reduced model more tractable. This method was expanded in the “Lift & Learn” framework [69] and operator inference techniques [70, 71], leveraging physics-informed machine learning for large-scale nonlinear dynamical systems.

Another advancement aimed at improving the efficiency of ROMs is the development of empirical interpolation methods (EIM). EIM was introduced to deal with non-affine parameter dependencies and nonlinearities [72, 73]. EIM constructs an approximation of nonlinear or non-affine terms by selecting interpolation points and functions to form an interpolation model. EIM has been widely used to construct efficient ROMs for nonaffine and nonlinear PDEs [73, 13, 74, 75, 76, 77, 30, 68, 78, 79]. Several attempts have been made to extend the EIM in various ways. The best-points interpolation method (BPIM) [26, 80] employs POD to generate the basis set and least squares to compute the interpolation point set. Generalized empirical interpolation method (GEIM) [81, 82] generalizes EIM by replacing the pointwise function evaluations by more general measures defined as linear functionals.

The first-order empirical interpolation method (FOEIM), introduced in [83, 56, 84], extends the standard EIM by using partial derivatives of parametrized nonlinear functions to generate additional basis functions and interpolation points. FOEIM has been further extended to a class of high-order empirical interpolation methods, which use higher-order partial derivatives to enrich the basis functions and interpolation points [85]. High-order EIM offers more flexible and accurate approximations compared to standard EIM, significantly improving the accuracy of hyper-reduced ROMs by capturing non-affine and nonlinear behaviors while maintaining computational efficiency.

In this paper, we introduce a generative reduced basis (RB) approach to constructing reduced-order models. Central to our approach is the construction of generative RB spaces, which offer a rapidly converging approximation of the solution manifold. We introduce the generative snapshot method to generate significantly larger sets of snapshots from a small initial set of solution snapshots. This method enriches the RB spaces without requiring additional FOM solutions, thereby enabling more accurate and efficient approximations of the solution manifold. The method complements existing model reduction techniques such as POD, greedy sampling, adaptive RB methods, optimal transport methods, nonlinear manifold methods, and non-intrusive and data-driven ROMs.

The proposed approach integrates several key components to enhance the accuracy and efficiency of ROMs. First, a Galerkin projection of the full-order model onto the generative RB spaces forms the reduced-order model. Second, we develop a posteriori error estimates that are inexpensive and tight. These error estimates are instrumental in guiding a greedy sampling algorithm, which effectively explores the parameter space and selects parameter points to optimize the accuracy of ROMs. Moreover, the approach leverages an offline-online decomposition to ensure computational efficiency.

Through a series of numerical experiments, we show that the generative snapshot method produces enriched RB spaces approximating the solution manifold far more accurately than the standard RB space. Furthermore, generative RB methods significantly improve both the accuracy and reliability of reduced-order models (ROM). Our results show that the generative RB approach not only accelerates the convergence of ROMs but also provides tight error bounds, making it particularly effective for high-dimensional and complex parametric problems.

The paper is organized as follows. In Section 2, we provide an overview of dimensionality reduction methods for constructing linear approximation

spaces. In Section 3, we introduce the generative snapshot method and present numerical results demonstrating its effectiveness. We propose a generative reduced basis method for affine linear PDEs in Section 4 and present numerical results to demonstrate the method in Section 5. Finally, in Section 6, we conclude with remarks on future work.

2. Linear Approximation Spaces

2.1. Parametric Solution Manifold

Let $\Omega \subset \mathbb{R}^D$ represent the physical domain, where $\mathbf{x} \in \Omega$ denotes the spatial coordinate. This physical domain may represent, for example, the geometry of a region in which a physical process (e.g., fluid flow, heat transfer, or structural deformation) takes place. Let $\mathcal{D} \subset \mathbb{R}^P$ denote the parameter domain, where $\boldsymbol{\mu}$ represents a set of P -dimensional parameters. These parameters encapsulate a wide range of physical, material, or geometrical properties of the system under consideration.

The function $u(\mathbf{x}, \boldsymbol{\mu})$ is the solution of a parametrized partial differential equation (PDE), which could be linear or nonlinear, time-dependent or time-independent. We define the solution manifold \mathcal{M} as the set of all possible solutions corresponding to every admissible parameter configuration in \mathcal{D} :

$$\mathcal{M} = \{u(\boldsymbol{\mu}), \forall \boldsymbol{\mu} \in \mathcal{D}\}, \quad (1)$$

where each element $u(\boldsymbol{\mu}) \in X$ represents the spatial solution $u(\mathbf{x}, \boldsymbol{\mu})$ for a particular parameter point $\boldsymbol{\mu}$. Here X is an appropriate Hilbert space equipped with an inner product $(\cdot, \cdot)_X$ and norm $\|v\|_X = \sqrt{(v, v)_X}$. The manifold \mathcal{M} can be viewed as a high-dimensional object that captures the full variability of the solution across the parameter domain. This high-dimensional nature presents significant computational challenges, as computing the full solution manifold requires solving the PDE for many different parameter values, which can be computationally prohibitive in real-time or many-query contexts, such as optimization or uncertainty quantification.

Let $\Xi_K = \{\hat{\boldsymbol{\mu}}_k \in \mathcal{D}\}_{k=1}^K$ be a set of K distinct parameter points sampled from the parameter domain. These points are used to compute corresponding solutions to the parametrized PDE, $u(\hat{\boldsymbol{\mu}}_k)$, which are used to define the following finite-dimensional space

$$\mathcal{M}_K = \text{span}\{u(\hat{\boldsymbol{\mu}}_k), 1 \leq k \leq K\}. \quad (2)$$

We assume that K is a large number such that the finite-dimensional space \mathcal{M}_K can approximate well any function in the solution manifold \mathcal{M} . However, constructing the space \mathcal{M}_K is computationally expensive, since it requires a large number of solutions. The primary purpose of the finite-dimensional space \mathcal{M}_K is to assess the quality of a RB space.

2.2. Kolmogorov n -Width

Let $V_M = \text{span}\{v_m, 1 \leq m \leq M\}$ be an approximation space of M dimension. We consider linear approximation in which any function $v \in V_M$ can be expressed as a linear combination of its basis functions, $v(\mathbf{x}) = \sum_{m=1}^M \alpha_m v_m(\mathbf{x})$, where $\alpha_m, 1 \leq m \leq M$, are real coefficients. For any given function $w \in X$, its best approximation in the space V_M is defined as

$$v^* = \arg \inf_{v \in V_M} \|v - w\|_X. \quad (3)$$

The best approximation can be computed as $v^* = \sum_{m=1}^M \alpha_m^* v_m$, where $\boldsymbol{\alpha}^* = \arg \inf_{\boldsymbol{\alpha} \in \mathbb{R}^M} \|\sum_{m=1}^M \alpha_m v_m - w\|_X$. To assess the accuracy of the space V_M in approximating the solution space \mathcal{M}_K , we define the following error metric:

$$d(V_M, \mathcal{M}_K) = \sup_{u \in \mathcal{M}_K} \inf_{v \in V_M} \|v - u\|_X. \quad (4)$$

This quantity measures the worst-case approximation error by calculating the maximum deviation between the solutions in \mathcal{M}_K and their best approximations within the space V_M . The smaller the value of the error metric the more accurate the space V_M is in approximating the functions in \mathcal{M}_K .

For a fixed dimension M , we wish to find the space $V_M^* \in X$ of dimension M that minimizes the worst-case approximation error across the entire solution manifold \mathcal{M}_K . Mathematically, this optimal approximation space is defined as

$$V_M^* = \arg \inf_{V_M} \sup_{u \in \mathcal{M}_K} \inf_{v \in V_M} \|v - u\|_X. \quad (5)$$

The associated error metric $d(V_M^*, \mathcal{M}_K)$ is known as the Kolmogorov n -width. The Kolmogorov n -width characterizes the smallest possible worst-case error that can be achieved using any M -dimensional approximation space. This provides a fundamental limit on the performance of any linear approximation method of fixed dimension M . If the Kolmogorov n -width converges rapidly to zero as M increases, it implies that the solution manifold \mathcal{M}_K is close to being representable by a low-dimensional linear subspace. Conversely, if the Kolmogorov n -width converges slowly, it indicates that solution manifold is inherently complex and high-dimensional.

2.3. Proper Orthogonal Decomposition

While the Kolmogorov n -width gives a powerful theoretical limit, finding the optimal approximation space that achieves this bound is generally not computable in practice. The concept of finding the best approximation space is closely related to Proper Orthogonal Decomposition (POD). POD provides a practical method for constructing an approximation space V_M that approximates the optimal space V_M^* by identifying the most energetic modes in the solution manifold. These modes correspond to the principal components of the solution manifold and can be obtained by applying singular value decomposition (SVD) to the snapshot data.

POD generates an orthogonal basis that minimizes the projection error in the L_2 norm. Mathematically, the POD basis functions solve the following minimization problem

$$\min_{V_M} \sum_{k=1}^K \left\| u(\boldsymbol{\mu}_k) - \sum_{m=1}^M (u(\boldsymbol{\mu}_k), v_m)_X v_m \right\|_X^2 \quad (6)$$

where V_M is constrained to be an orthogonal space of dimension M . This minimization problem amounts to solving the following eigenvalue problem

$$\mathbf{C}\mathbf{a} = \lambda\mathbf{a} \quad (7)$$

where $\mathbf{C} \in \mathbb{R}^{K \times K}$ is the covariance matrix with entries $C_{kk'} = (u(\boldsymbol{\mu}_k), u(\boldsymbol{\mu}_{k'}))_X$, $1 \leq k, k' \leq K$. The eigenvectors provide the coefficients that describe the linear combination of the snapshots that form the optimal POD basis. Once the eigenvalue problem has been solved, the POD basis functions can be computed as a linear combination of the original snapshots. The m -th POD basis function v_m is constructed as

$$v_m = \sum_{k=1}^K a_{mk} u(\boldsymbol{\mu}_k), \quad (8)$$

where a_{mk} are components of the eigenvector associated with the m -th largest eigenvalue.

2.4. Greedy Sampling Algorithm

While POD provides an orthogonal basis that closely approximates the optimal space V_M^* , constructing this basis requires access to the entire solution

manifold \mathcal{M}_K . One of the primary challenges in constructing the POD basis is the high computational cost of generating the snapshots. One effective approach to reduce the number of required snapshots is the use of greedy algorithm. This method begins with a small set of snapshots and adds new ones in an iterative fashion by selecting those that maximally reduce the approximation error at each step. Greedy algorithm relies on inexpensive error estimates in order to effectively explore the parameter space.

The greedy algorithm starts with a small set of parameter points $\{\boldsymbol{\mu}_i\}_{i=1}^n$ randomly selected in the parameter domain. These initial parameter points are used to compute the corresponding solutions, $\{u(\boldsymbol{\mu}_i)\}_{i=1}^n$, which span the initial RB space $W_n = \text{span}\{u(\boldsymbol{\mu}_i), 1 \leq i \leq n\}$. It finds the next parameter point $\boldsymbol{\mu}_{n+1}$ that maximizes an error estimate $\varepsilon_n(\boldsymbol{\mu})$ over a training set Ξ_{train} :

$$\boldsymbol{\mu}_{n+1} = \arg \max_{\boldsymbol{\mu} \in \Xi_{\text{train}}} \varepsilon_n(\boldsymbol{\mu}), \quad (9)$$

where $\varepsilon_n(\boldsymbol{\mu})$ is an estimate of the true error $\|u(\boldsymbol{\mu}) - u_n(\boldsymbol{\mu})\|_X$, with $u_n(\boldsymbol{\mu}) \in W_n$ being an appropriate approximation to $u(\boldsymbol{\mu})$. The training sample Ξ_{train} can be either a very fine grid in the parameter domain or an exhaustive list of randomly selected parameter points. Then the RB space W_{n+1} is augmented by adding $u(\boldsymbol{\mu}_{n+1})$ to W_n . This process is repeated until $\varepsilon_N(\boldsymbol{\mu})$ is less than a specified tolerance, where N is the total number of basis functions in the final RB space $W_N = \text{span}\{u(\boldsymbol{\mu}_i), 1 \leq i \leq N\}$.

Although the greedy algorithm is widely used for constructing RB spaces, it has several limitations. One of the key challenges lies in the computation of error estimates for numerous parameter points within the training set. For the algorithm to be effective, these error estimates must be inexpensive, rigorous, and tight. However, achieving all three properties simultaneously is often difficult—error estimates that are inexpensive may lack rigor or accuracy, while rigorous and tight estimates can be computationally expensive. Each time a new parameter point is selected, the corresponding solution must be computed, which requires solving the parametrized PDE. This can be costly, especially when many iterations of the greedy algorithm are required. In high-dimensional parameter spaces, the size of the training set grows exponentially with the number of parameters. This makes it difficult to sample the parameter space adequately, leading to potential gaps in the training set. If the training set does not adequately cover the parameter space, the algorithm might fail to capture critical parameter regions where the solution exhibits significant variation. As a result, the reduced ba-

sis might not provide accurate approximations for certain parameter values. The convergence of the algorithm is strongly dependent on the smoothness and structure of the solution manifold. For certain problems with complex solution manifolds, the greedy algorithm may converge slowly, necessitating a large number of basis functions to achieve the desired accuracy.

3. Generative Snapshot Method

We introduce a method for generating an expanded set of snapshots from a small initial set of solutions by applying multivariate nonlinear transformations. These transformations enrich the original set of solutions, creating new snapshots that capture more complex patterns within the solution manifold. After generating these new snapshots, POD is applied to construct generative RB spaces. The key advantage of this method is that it significantly enlarges the snapshot space without requiring additional solutions. The method allows for more accurate approximations of the solution manifold by producing high-quality RB spaces. To demonstrate the effectiveness of the generative snapshot method, we present a series of numerical examples that compare the performance of generative RB spaces to that of the traditional RB space.

3.1. Multivariate Nonlinear Transformations

Let $\sigma(v)$ be a proper nonlinear function of a scalar variable v . We assume that σ is smooth and at least twice differentiable with respect to v , and that the inverse function $\sigma^{-1}(w)$ exists. We then introduce the following two-variable function

$$G(v_1, v_2) = \sigma(v_1) + \frac{\partial \sigma(v_1)}{\partial v}(v_2 - v_1) \quad (10)$$

and define the corresponding space

$$\mathcal{G}_{N^2} = \text{span}\{\rho_{mn} \equiv \sigma^{-1}(G(\xi_n, \xi_m)), 1 \leq n, m \leq N\}. \quad (11)$$

Here $\{\xi_n \equiv u(\boldsymbol{\mu}_n)\}_{n=1}^N$ is the set of N solutions defining the RB space W_N :

$$W_N = \text{span}\{\xi_n \equiv u(\boldsymbol{\mu}_n), 1 \leq i \leq N\}. \quad (12)$$

It can be easily shown that $W_N \subset \mathcal{G}_{N^2}$. The dimension of \mathcal{G}_{N^2} may far exceed N , but it is less than or equal to N^2 .

We further introduce a three-variable function to capture higher-order nonlinear interactions:

$$H(v_1, v_2, v_3) = \sigma(v_1) + \frac{\partial\sigma(v_1)}{\partial v}(v_2 - v_1) + \frac{1}{2} \frac{\partial^2\sigma(v_1)}{\partial v^2}(v_2 - v_1)(v_3 - v_1), \quad (13)$$

and define the associated space

$$\mathcal{H}_{N^3} = \text{span}\{\varrho_{mnp} \equiv \sigma^{-1}(H(\xi_n, \xi_m, \xi_p)), 1 \leq n, m, p \leq N\}. \quad (14)$$

It can be demonstrated that $W_N \subset \mathcal{G}_{N^2} \subset \mathcal{H}_{N^3}$. The space \mathcal{G}_{N^2} contains N^2 functions, while \mathcal{H}_{N^3} extends this by incorporating N^3 functions, offering a richer and more accurate representation of the solution manifold.

This hierarchical structure of spaces $W_N \subset \mathcal{G}_{N^2} \subset \mathcal{H}_{N^3}$ enables a flexible approach for generating snapshots, allowing for progressively more detailed approximations of the solution space and construction of efficient and accurate ROMs. In addition to enhancing ROM accuracy, this approach also enables the development of efficient error estimation techniques. The hierarchical structure facilitates the generation of tight error bounds by comparing the approximations across the nested spaces.

3.2. Generative Reduced Basis Spaces

Due to the potentially large number of snapshots in \mathcal{G}_{N^2} and \mathcal{H}_{N^3} , generating basis functions via POD may become computationally intensive. We can reduce the number of snapshots by using the nearest parameter points as follows. We compute the distances $d_{nn'} = \|\boldsymbol{\mu}_n - \boldsymbol{\mu}_{n'}\|$, $1 \leq n, n' \leq N$, between each pair of parameter points $\boldsymbol{\mu}_n$ and $\boldsymbol{\mu}_{n'}$ in S_N . For any given $\boldsymbol{\mu}_n \in S_N$, we define $S_L(\boldsymbol{\mu}_n)$ a set of exactly L parameter points that are closest to $\boldsymbol{\mu}_n$. For any solution $\xi_n \in W_N$, we define $W_L(\xi_n) = \{u(\boldsymbol{\mu}_l), \forall \boldsymbol{\mu}_l \in S_L(\boldsymbol{\mu}_l)\}$, which contains exactly L solutions. We then introduce the following sets of snapshots

$$\begin{aligned} \mathcal{G}_{NL} &= \text{span}\{\rho_{nl} \equiv \sigma^{-1}(G(\xi_n, \xi_l)), \forall \xi_l \in W_L(\xi_n), 1 \leq n \leq N\}, \\ \mathcal{H}_{NL^2} &= \text{span}\{\varrho_{nlv} \equiv \sigma^{-1}(H(\xi_n, \xi_l, \xi_{l'})), \forall \xi_l, \xi_{l'} \in W_L(\xi_n), 1 \leq n \leq N\}. \end{aligned} \quad (15)$$

These snapshot sets satisfy $W_N \subset \mathcal{G}_{NL} \subset \mathcal{H}_{NL^2} \subset \mathcal{H}_{N^3}$ and contain NL and NL^2 functions, respectively.

We apply POD to both \mathcal{G}_{NL} and \mathcal{H}_{NL^2} in order to compress the functions within these spaces. Thus, we obtain two sets of orthogonal basis functions

that efficiently approximate the solution manifold. These basis functions provide a more compact representation for the reduced basis approximation while preserving accuracy. Specifically, the compressed spaces corresponding to \mathcal{G}_{NL} and \mathcal{H}_{NL^2} are given by

$$\Phi_N^{M_1} = \text{span}\{\phi_m, 1 \leq m \leq M_1\}, \quad \Psi_N^{M_2} = \text{span}\{\psi_m, 1 \leq m \leq M_2\}, \quad (16)$$

where the superscripts M_1 and M_2 denote the dimensions of the two RB spaces, and the subscript N indicates the number of solutions used to construct these spaces. The dimension M_1 (or M_2) is chosen such that the sum of the eigenvalues corresponding to the first M_1 (or M_2) POD modes captures most of the total sum of all the eigenvalues. Both M_1 and M_2 can be far greater than N . Typically, M_2 is greater than M_1 due to the fact $\mathcal{G}_{NL} \subset \mathcal{H}_{NL^2}$.

Due to $W_N \subset \mathcal{G}_{NL} \subset \mathcal{H}_{NL^2}$, we can expect that the error metrics for the three different RB spaces satisfy the below relationship

$$d(\Psi_N^{M_2}, \mathcal{M}_K) \leq d(\Phi_N^{M_1}, \mathcal{M}_K) \leq d(W_N, \mathcal{M}_K). \quad (17)$$

Hence, the generative RB spaces should provide better approximations than the standard RB space. The convergence rates of these error metrics as a function of N reflect the performance of the generative RB spaces, $\Phi_N^{M_1}$ and $\Psi_N^{M_2}$, relative to the standard RB space W_N .

3.3. Nonlinear Activation Functions

The nonlinear function σ plays a crucial role in the generative snapshot method, as it facilitates the transformation of a small set of original solutions into a significantly larger set of enriched snapshots through multivariate nonlinear operations. By introducing nonlinearity into the generated snapshots, σ enables the new set to capture more complex and intricate relationships within the solution manifold that are not easily represented by the original solutions alone. This nonlinearity is essential for expanding the expressiveness of the reduced basis (RB) space, as it allows the method to approximate the solution manifold more effectively.

The function σ must satisfy two key requirements to ensure the method's effectiveness. First, σ must be at least twice differentiable to ensure that the transformations and expansions generated by σ are smooth and stable, allowing for accurate computation of higher-order interactions when constructing enriched snapshots. Second, the inverse function σ^{-1} must exist and be

well-defined, ensuring that the nonlinear transformations can be consistently inverted when required. The existence of an inverse is crucial for defining the transformed snapshot spaces and maintaining consistency in the generation of new basis functions.

The function σ not only transforms individual solutions but also enables the generation of snapshots that incorporate higher-order correlations between multiple solutions. For example, in the generative snapshot method, the nonlinear function is applied to pairs or triples of solutions to create spaces of N^2 or N^3 snapshots. This multivariate expansion enhances the richness of the snapshot space and improves the approximation accuracy of ROMs by capturing interactions that would otherwise be missed in a purely linear approximation approach. It allows the generative snapshot method to construct high-quality RB spaces that significantly improve the accuracy and generalization capabilities of ROMs.

Beyond these fundamental requirements, the choice of σ can significantly impact the effectiveness of the method. A carefully chosen nonlinear function can balance complexity and computational efficiency, ensuring that the enriched snapshot set provides substantial improvements in accuracy without introducing excessive computational overhead. Common candidates for σ include smooth polynomial functions, sigmoidal functions, exponential functions, or even more complex functions derived from machine learning models, depending on the nature of the solution space.

In this paper, we explore several options for the nonlinear function σ , which play a crucial role in the generative snapshot method by introducing the necessary nonlinearity to capture the solution manifold. As shown in Table 1, we consider a variety of commonly used activation functions, including hyperbolic tangent, sigmoid, arctangent, softplus, exponential, and quadratic functions. These functions are smooth and continuously differentiable, making them well-suited for mathematical models that require gradient calculations and smooth transformations. They are widely employed in neural networks due to their ability to model nonlinear relationships, enabling the network to learn complex data distributions. In the context of the generative snapshot method, these nonlinear functions are natural candidates for transforming the original set of solutions into a larger, enriched snapshot set that accurately captures the solution manifold.

$\sigma(x)$	$\partial\sigma(x)/\partial x$	$\partial^2\sigma(x)/\partial x^2$	$\sigma^{-1}(x)$
$\tanh(x)$	$1 - \sigma^2(x)$	$2\sigma(x)(\sigma^2(x) - 1)$	$\frac{1}{2} \ln\left(\frac{1+x}{1-x}\right)$
$\frac{1}{1+e^{-x}}$	$\sigma(x)(1 - \sigma(x))$	$\sigma(x)(1 - \sigma(x))(1 - 2\sigma(x))$	$\ln\left(\frac{x}{1-x}\right)$
$\arctan(x)$	$\frac{1}{1+x^2}$	$\frac{-2x}{(1+x^2)^2}$	$\tan(x)$
$\ln(1 + e^x)$	$\frac{1}{1+e^{-x}}$	$\frac{e^x}{(1+e^x)^2}$	$\ln(e^x - 1)$
e^x	e^x	e^x	$\ln(x)$
x^2	$2x$	2	\sqrt{x}

Table 1: Nonlinear activation functions, their first and second-order derivatives, and inverse functions.

3.4. One-Dimensional Parametrized Function

We present numerical results from a simple test case to assess the performance of the generative snapshot method. The test case involves the following parametrized function

$$u(x, \mu) = \frac{x}{(\mu + 1) \left(1 + \sqrt{\frac{\mu+1}{\exp(62.5)}} \exp\left(\frac{125x^2}{\mu+1}\right) \right)} \quad (18)$$

in a physical domain $\Omega = [0, 2]$ and parameter domain $\mathcal{D} = [0, 10]$. We choose the function space $X = L^2(\Omega)$ with the inner product $(w, v)_X = \int_{\Omega} wv dx$. Figure 1 shows the plots of u for various values of μ . The solution has a sharp shock profile at $x = 0.5$ for $\mu = 0$. As μ increases, this shock profile moves to the right boundary and smears out.

The sample S_N consists of N parameter points from an extended Chebyshev distribution over the parameter domain \mathcal{D} . Thus, the standard RB space W_N consists of N snapshots that correspond to these extended Chebyshev points. The generative RB spaces, $\Phi_N^{M_1}$ and $\Psi_N^{M_2}$, are also constructed from these N solutions by using the generative snapshot method for two different values of L , which are $L = \min(4, N)$ and $L = \min(8, N)$. We assess the performance of these RB spaces by studying the convergence of the error

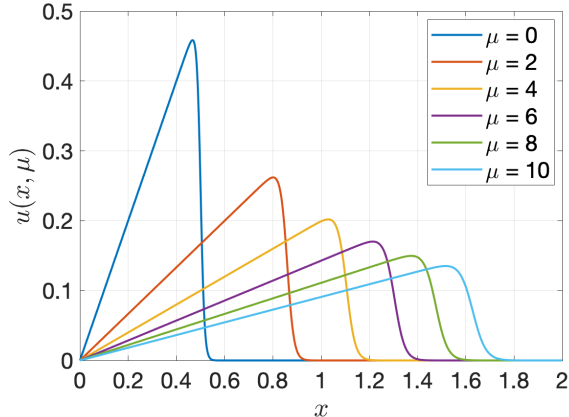


Figure 1: Plots of $u(x, \mu)$ defined in (18) as a function of x for different values of μ .

metric defined in Equation (4) as a function of N . To this end, we employ $K = 200$ parameter points sampled uniformly over \mathcal{D} . Consequently, the discrete solution manifold \mathcal{M}_K is composed of 200 snapshots.

Figures 2 and 3 display the error metric for the standard and generative RB spaces as a function of N for $L = \min(4, N)$ and $L = \min(8, N)$, respectively. As expected, increasing N reduces the error in all RB spaces. However, the generative RB spaces show significantly lower errors compared to the standard RB space for all choices of the nonlinear function, with the exception of the quadratic function. For the hyperbolic tangent, sigmoid, Softplus, and arctangent, and exponential functions, the error decreases more rapidly in the generative RB spaces as N increases. This demonstrates the ability of these transformations to enrich the RB spaces. In contrast, the quadratic function does not offer the same degree of error reduction. Furthermore, increasing L leads to reduction in the error for the space $\Phi_N^{M_1}$, but it has very little impact on the space $\Phi_N^{M_2}$. This indicates that the higher-order correlations are sufficient for improving accuracy, and further increasing the number of snapshots offers diminishing returns.

In summary, the results show that the generative RB spaces based on higher-order transformations (such as $\Psi_N^{M_2}$) consistently outperform both the standard RB space and lower-order generative spaces (such as $\Phi_N^{M_1}$). This performance gap becomes more pronounced as N increases. This highlights the importance of selecting appropriate nonlinear functions and transformation orders when constructing generative RB spaces.

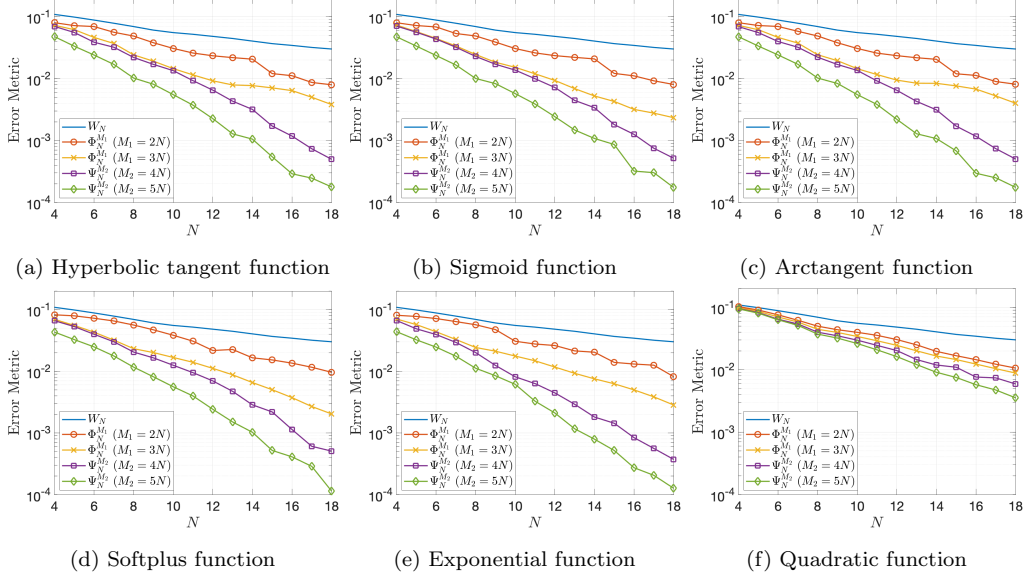


Figure 2: The error metric for the standard RB space W_N and the generative RB spaces $\Phi_N^{M_1}$ and $\Psi_N^{M_2}$ as a function of N for $L = \min(4, N)$.

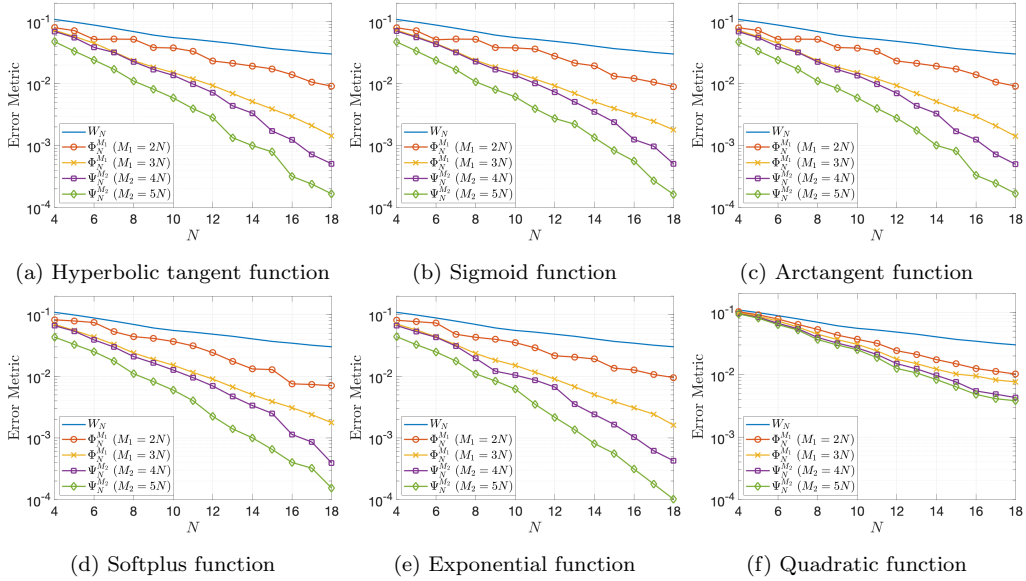


Figure 3: The error metric for the standard RB space W_N and the generative RB spaces $\Phi_N^{M_1}$ and $\Psi_N^{M_2}$ as a function of N for $L = \min(8, N)$.

3.5. Two-Dimensional Parametrized Function

We present numerical results from a two-dimensional test case to assess the performance of the generative snapshot method. The test case involves the following parametrized function

$$u(\mathbf{x}, \boldsymbol{\mu}) = x_1 x_2 \tanh((1 - x_1)\mu_1) \tanh((1 - x_2)\mu_2) \quad (19)$$

in a physical domain $\Omega = [0, 1]^2$ and parameter domain $\mathcal{D} = [1, 50]^2$. We choose the function space $X = L^2(\Omega)$. Figure 4 shows four instances of $u(\mathbf{x}, \boldsymbol{\mu})$ corresponding to the four corners of the parameter domain. As $\boldsymbol{\mu}$ increases, the solution develops sharp boundary layers.

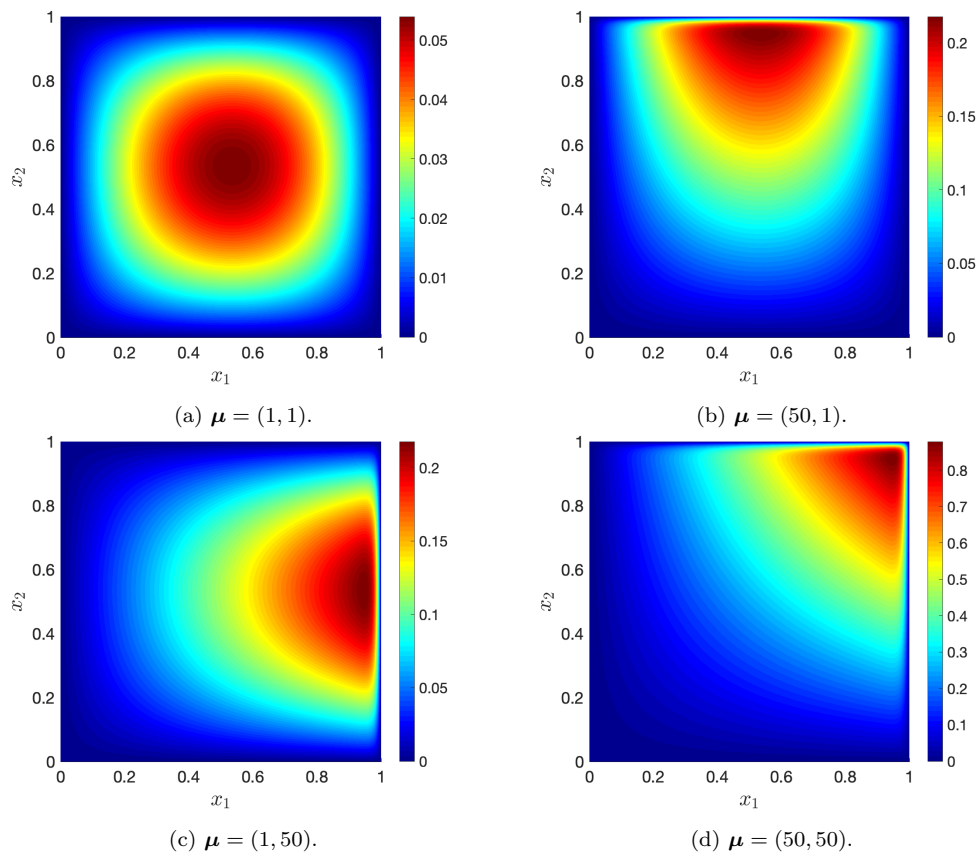


Figure 4: Plots of $u(\mathbf{x}, \boldsymbol{\mu})$ defined in (19) for four different values of $\boldsymbol{\mu}$.

We choose for S_N a set of $\sqrt{N} \times \sqrt{N}$ parameter points from the extended Chebyshev distribution over the parameter domain \mathcal{D} . The generative RB

spaces, $\Phi_N^{M_1}$ and $\Psi_N^{M_2}$, are constructed from these N solutions by using the generative snapshot method for $L = \min(5, N)$. We employ 40×40 parameter points sampled uniformly over \mathcal{D} to construct the discrete solution manifold \mathcal{M}_K of $K = 1600$ snapshots.

We assess the performance of the RB spaces by showing the convergence of their error metric as a function of N in Figure 5. As expected, increasing N consistently reduces the error across all RB spaces. However, the generative RB spaces show significantly lower errors compared to the standard RB space for all choices of the nonlinear function. Among the tested nonlinear activation functions, the hyperbolic tangent, sigmoid, and arctangent show very similar convergence behaviors for the error metric. These functions show a steady reduction in error as N increases, indicating their effectiveness in capturing non-linearity within the solution space. The softplus and exponential activation functions, on the other hand, result in even faster convergence, yielding lower errors compared to the hyperbolic tangent, sigmoid, and arctangent functions.

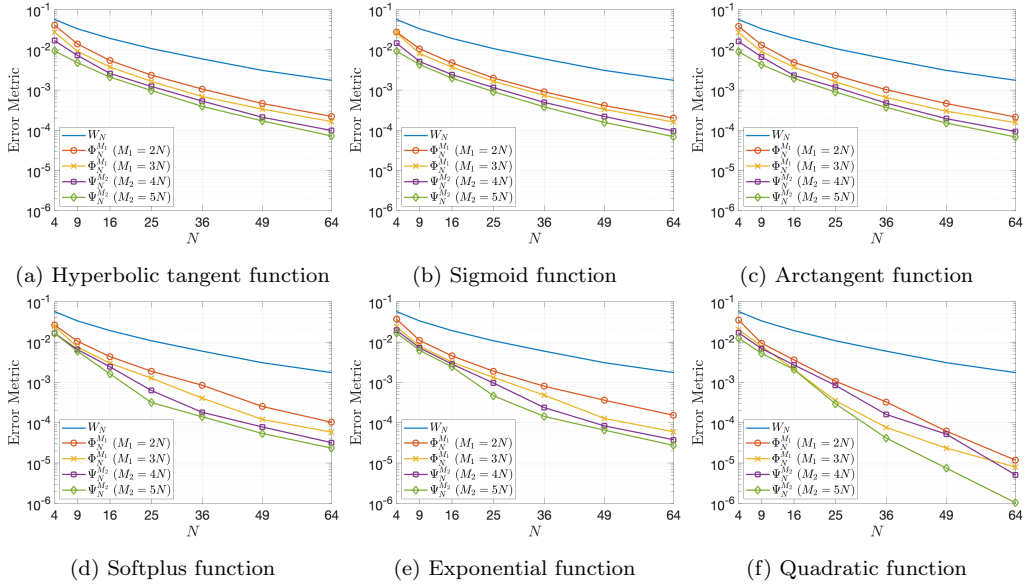


Figure 5: The error metric for the standard RB space W_N and the generative RB spaces $\Phi_N^{M_1}$ and $\Psi_N^{M_2}$ as a function of N for $L = \min(5, N)$.

Interestingly, in contrast to the previous example, the quadratic function exhibits the fastest convergence and the smallest error in this case. This indicates that while the performance of the quadratic function may vary

depending on the characteristics of the underlying solution manifold, it can be highly effective in specific contexts where polynomial-based transformations are sufficient to capture the relevant features. For $N = 64$, the error for $\Psi_N^{M_2}$ with $M_2 = 5N$ is 1000 times smaller than the error for the standard RB space W_N . This highlights the exceptional performance of the generative RB space with quadratic transformations. The significant error reduction suggests that these higher-order transformations allow the generative RB space to capture the complex structure of the solution manifold more accurately.

Overall, these results confirm the advantages of using nonlinear transformations to expand the snapshot set and construct generative RB spaces. The ability of softplus and exponential functions to accelerate error convergence, combined with the strong performance of the quadratic function in this particular case, demonstrates the flexibility of the generative approach. The results also underscore the importance of selecting the appropriate nonlinear transformation based on the specific characteristics of the problem to be addressed, as the choice of σ can significantly influence both the convergence rate and the accuracy of the RB spaces.

3.6. Three-Dimensional Parametrized Function

In the last example, we consider the parametrized spherical Bessel function [86, 87, 88, 89]:

$$u(\mathbf{x}, \mu) = \frac{\sin(\mu\pi r)}{\mu\pi r} \exp\left(1 - \frac{1}{\sqrt{(1-r^3)^2 + 10^{-6}}}\right), \quad (20)$$

where $r = \sqrt{x_1^2 + x_2^2 + x_3^2}$ is the radial distance from the origin in the unit sphere domain Ω , and μ is the parameter defined in the range $\mathcal{D} = [1, 20]$. Spherical Bessel functions are commonly used in modeling wave propagation, oscillatory phenomena, and scattering problems, making this an ideal test case to evaluate the performance of RB spaces in handling highly oscillatory solutions.

Figure 6 shows the behavior of $u(\mathbf{x}, \mu)$ along the line $x_2 = x_3 = 0$ for several values of μ . As expected, the solution exhibits strong oscillations that depend on the parameter μ . For lower values of μ , the function displays more moderate oscillations, while for higher values, the frequency of oscillation increases significantly. This high-frequency behavior poses a challenge for the standard RB space, as accurately capturing such oscillations may require a large number of basis functions.

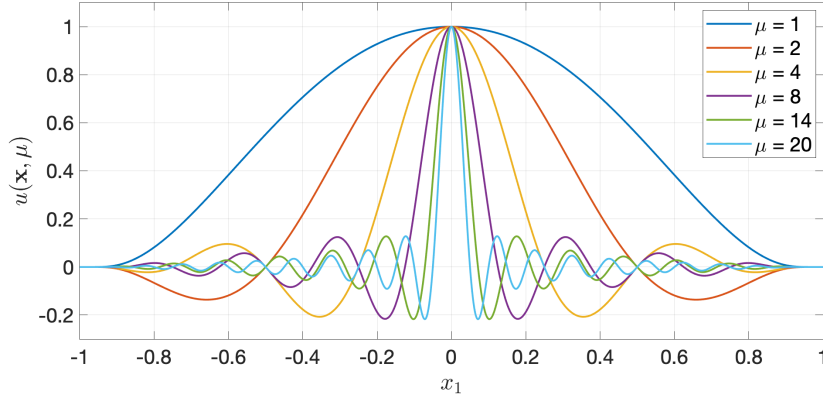


Figure 6: Plots of $u(\mathbf{x}, \mu)$ in (20) along the line $x_2 = x_3 = 0$ for different values of μ .

The parameter sample set S_N is drawn from an extended Chebyshev distribution over the parameter domain. The extended Chebyshev distribution is chosen to ensure better coverage of the parameter space, particularly in capturing regions where the solution manifold may exhibit more complex behavior. To define the discrete solution manifold \mathcal{M}_K , we employ $K = 100$ parameter points, which are sampled uniformly over the parameter domain. By discretizing the solution manifold in this way, we can assess the performance of the RB spaces to approximate the full solution space effectively. The combination of the extended Chebyshev distribution for S_N and the uniform sampling for \mathcal{M}_K ensures that both the training set and the test set are well distributed across the parameter domain.

Figure 7 presents the error metric as a function of the number of basis functions N for the standard and generative RB spaces. Across all subplots, the standard RB space consistently exhibits the highest error for all values of N , ranging from 0.45 to 0.065 as N increases from 4 to 14. This slow error reduction reflects the difficulty in capturing the highly oscillatory behavior of the spherical Bessel function. The error decreases with increasing N , but the rate of reduction is slow, highlighting the inefficiency of the standard RB space when dealing with complex oscillatory functions. The generative RB spaces significantly outperform the standard RB space, with much lower errors across the range of N . For $N = 14$, the error for $\Psi_N^{M_2}$ with $M_2 = 5N$ reaches values below 10^{-6} representing an improvement of four orders of magnitude compared to the standard RB space. This illustrates the effectiveness of the generative snapshot method in handling oscillatory solutions.

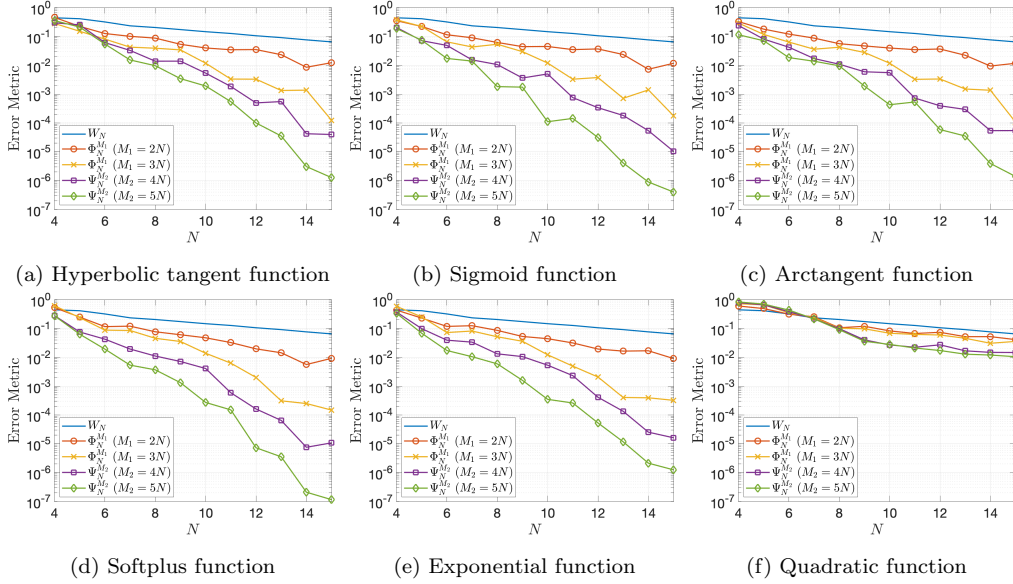


Figure 7: The error metric for the standard RB space W_N and the generative RB spaces $\Phi_N^{M_1}$ and $\Psi_N^{M_2}$ as a function of N for $L = \min(5, N)$.

The softplus and exponential functions show the most rapid error convergence among the nonlinear functions used in the generative RB spaces. They are highly effective at capturing the oscillatory behavior of the spherical Bessel function, making them particularly suited for complex problems with sharp transitions or high-frequency components. The hyperbolic tangent, sigmoid, and arctangent functions also perform well and provide substantial error reduction compared to the standard RB space. In contrast, the quadratic function shows the slowest error reduction among these nonlinear functions. This suggests that the quadratic function is insufficient to capture the complexity of the spherical Bessel function.

In summary, the results demonstrate the clear superiority of generative RB spaces over the standard RB space when applied to the spherical Bessel function, which poses a challenging test case due to its oscillatory nature. Among the nonlinear functions considered, the softplus and exponential transformations offer the best performance, achieving rapid error reduction and high accuracy. The $\Psi_N^{M_2}$ spaces consistently outperform the $\Phi_N^{M_1}$ spaces. Therefore, higher-order transformations lead to richer snapshot sets that can more accurately represent the oscillatory behavior of the spherical Bessel function, resulting in faster convergence and lower error.

4. Generative Reduced Basis Method

In this section, we introduce a generative reduced basis (RB) method to construct reduced-order models (ROMs) for affine linear PDEs. The method leverages the generative snapshot technique to construct enriched RB spaces. The generative RB method not only improves accuracy, but also provides *a posteriori* error estimates. These error estimates are used in a greedy algorithm to select parameter points to construct the generative RB spaces.

4.1. Finite Element Approximation

The weak formulation for a parametrized linear PDE can be stated as follows: given any $\boldsymbol{\mu} \in \mathcal{D} \subset \mathbb{R}^P$, we evaluate $s^e(\boldsymbol{\mu}) = \ell^O(u^e(\boldsymbol{\mu}); \boldsymbol{\mu})$, where $u^e(\boldsymbol{\mu}) \in X^e$ is the solution of

$$a(u^e(\boldsymbol{\mu}), v; \boldsymbol{\mu}) = \ell(v; \boldsymbol{\mu}), \quad \forall v \in X^e. \quad (21)$$

Here \mathcal{D} is the parameter domain in which our P -tuple (input) parameter $\boldsymbol{\mu}$ resides; $X^e(\Omega)$ is an appropriate Hilbert space on Ω ; Ω is a bounded domain in \mathbb{R}^d with Lipschitz continuous boundary $\partial\Omega$; $\ell(\cdot; \boldsymbol{\mu})$, $\ell^O(\cdot; \boldsymbol{\mu})$ are X^e -continuous linear functionals; and $a(\cdot, \cdot; \boldsymbol{\mu})$ is a bilinear form of the parameterized PDE operator. In actual practice, we replace $u^e(\boldsymbol{\mu})$ with an approximate solution, $u(\boldsymbol{\mu})$, which resides in a finite element approximation space $X \subset X^e$ of *very* large dimension \mathcal{N} and satisfies

$$a(u(\boldsymbol{\mu}), v; \boldsymbol{\mu}) = \ell(v), \quad \forall v \in X. \quad (22)$$

We then evaluate the finite element output as

$$s(\boldsymbol{\mu}) = \ell^O(u(\boldsymbol{\mu})) . \quad (23)$$

We assume that the FE solution and output are indistinguishable from the exact solution and output at the accuracy level of interest.

For simplicity of exposition, we assume that both ℓ and ℓ^O are independent of $\boldsymbol{\mu}$. Furthermore, we assume that the bilinear form a may be expressed as an affine decomposition of the form

$$a(w, v; \boldsymbol{\mu}) = \sum_{q=1}^Q \Theta^q(\boldsymbol{\mu}) a^q(w, v) \quad (24)$$

where $a^q(\cdot, \cdot)$ are $\boldsymbol{\mu}$ -independent bilinear forms, and $\Theta^q(\boldsymbol{\mu})$ are $\boldsymbol{\mu}$ -dependent functions. These assumptions can be relaxed by using the empirical interpolation method [72, 73] or its high-order variants [83, 56].

4.2. Reduced Basis Approximation

The parameter sample $S_N = \{\boldsymbol{\mu}_n\}_{n=1}^N$ is generated using a greedy sampling algorithm, which will be discussed in detail later. Once the parameter sample set S_N is defined, we proceed to compute the FE solutions $\{u(\boldsymbol{\mu}_n)\}_{n=1}^N$ by solving the weak formulation (22) for each parameter point in S_N . Rather than relying solely on these original solutions to construct the traditional RB space W_N , we apply the generative snapshot method, as outlined in the previous section, to construct the generative RB spaces

$$\Phi_N^{M_1} = \text{span}\{\phi_m, 1 \leq m \leq M_1\}, \quad \Psi_N^{M_2} = \text{span}\{\psi_m, 1 \leq m \leq M_2\}. \quad (25)$$

These generative RB spaces incorporate additional snapshots generated through nonlinear transformations to significantly expand the solution space, thereby improving the accuracy of the RB approximation. Furthermore, we compute *a posteriori* error estimates by leveraging these enriched RB spaces, as discussed in the following section.

To develop the RB approximation of the FE formulation, we perform a Galerkin projection of equation (22) onto $\Phi_N^{M_1}$. Given a parameter point $\boldsymbol{\mu} \in \mathcal{D}$, we evaluate $s_{M_1}(\boldsymbol{\mu}) = \ell^O(u_{M_1}(\boldsymbol{\mu}))$, where $u_{M_1}(\boldsymbol{\mu}) \in \Phi_N^{M_1}$ is the solution of

$$a(u_{M_1}(\boldsymbol{\mu}), v; \boldsymbol{\mu}) = \ell(v), \quad \forall v \in \Phi_N^{M_1}. \quad (26)$$

We express $u_{M_1}(\boldsymbol{\mu}) = \sum_{j=1}^{M_1} \alpha_{M_1,j}(\boldsymbol{\mu})\phi_j$ to evaluate the RB output as

$$s_{M_1}(\boldsymbol{\mu}) = (\boldsymbol{l}_{M_1}^O)^T \boldsymbol{\alpha}_{M_1}(\boldsymbol{\mu}) \quad (27)$$

where $\boldsymbol{\alpha}_{M_1}(\boldsymbol{\mu}) \in \mathbb{R}^{M_1}$ as the solution of the following linear system

$$\left(\sum_{q=1}^Q \Theta^q(\boldsymbol{\mu}) \mathbf{A}_{M_1}^q \right) \boldsymbol{\alpha}_{M_1}(\boldsymbol{\mu}) = \boldsymbol{l}_{M_1}. \quad (28)$$

Here the matrices $\mathbf{A}_{M_1}^q \in \mathbb{R}^{M_1 \times M_1}$, $1 \leq q \leq Q$, and the vectors $\boldsymbol{l}_{M_1}, \boldsymbol{l}_{M_1}^O \in \mathbb{R}^{M_1}$ are computed as

$$A_{M_1,ij}^q = a^q(\phi_i, \phi_j), \quad l_{M_1,i} = \ell(\phi_i), \quad l_{M_1,i}^O = \ell^O(\phi_i), \quad (29)$$

for $1 \leq i, j \leq M_1$. The RB system (28) is derived from (26) by choosing $v = \phi_i$, $1 \leq i \leq M_1$, and invoking the affine decomposition (24).

Since $\mathbf{A}_{M_1}^q$, $1 \leq q \leq Q$, and $\boldsymbol{l}_{M_1}, \boldsymbol{l}_{M_1}^O$ are independent of $\boldsymbol{\mu}$, they can be pre-computed and stored in the offline stage. In the online stage, for any $\boldsymbol{\mu} \in \mathcal{D}$, we solve the system (28) for $\boldsymbol{\alpha}_{M_1}(\boldsymbol{\mu})$ with $O(QM_1^2 + M_1^3)$ operation counts and evaluate $s_{M_1}(\boldsymbol{\mu})$ from (27) with $O(M_1)$ operation counts.

4.3. A Posteriori Error Estimation

The error estimates provide a way to quantify the accuracy of the RB output and solution. The proposed error estimates rely on a more refined RB approximation, which is constructed using the larger generative RB space $\Psi_N^{M_2}$. Specifically, we evaluate the refined RB output as

$$s_{M_2}(\boldsymbol{\mu}) = (\mathbf{l}_{M_2}^O)^T \boldsymbol{\beta}_{M_2}(\boldsymbol{\mu}) \quad (30)$$

where $\boldsymbol{\beta}_{M_2}(\boldsymbol{\mu}) \in \mathbb{R}^{M_2}$ as the solution of the following linear system

$$\left(\sum_{q=1}^Q \Theta^q(\boldsymbol{\mu}) \mathbf{A}_{M_2}^q \right) \boldsymbol{\beta}_{M_2}(\boldsymbol{\mu}) = \mathbf{l}_{M_2}. \quad (31)$$

Here the matrices $\mathbf{A}_{M_2}^q \in \mathbb{R}^{M_2 \times M_2}$, $1 \leq q \leq Q$, and the vectors $\mathbf{l}_{M_2}, \mathbf{l}_{M_2}^O \in \mathbb{R}^{M_2}$ are computed as

$$A_{M_2,ij}^q = a^q(\psi_i, \psi_j), \quad l_{M_1,i} = \ell(\psi_i), \quad l_{M_2,i}^O = \ell^O(\psi_i), \quad (32)$$

for $1 \leq i, j \leq M_2$.

The error estimate for $\epsilon_{M_1}^s(\boldsymbol{\mu}) = |s(\boldsymbol{\mu}) - s_{M_1}(\boldsymbol{\mu})|$ is evaluated as

$$\bar{\epsilon}_{M_1 M_2}^s(\boldsymbol{\mu}) = |s_{M_2}(\boldsymbol{\mu}) - s_{M_1}(\boldsymbol{\mu})|, \quad (33)$$

where $s_{M_2}(\boldsymbol{\mu})$ is the output computed using $\Psi_N^{M_2}$, and $s_{M_1}(\boldsymbol{\mu})$ is the output obtained from the smaller RB space $\Phi_N^{M_1}$. Similarly, the estimate for the RB solution error $\epsilon_{M_1}^u(\boldsymbol{\mu}) = \|u(\boldsymbol{\mu}) - u_{M_1}(\boldsymbol{\mu})\|_X$ is computed as

$$\bar{\epsilon}_{M_1 M_2}^u(\boldsymbol{\mu}) = \|u_{M_2}(\boldsymbol{\mu}) - u_{M_1}(\boldsymbol{\mu})\|_X, \quad (34)$$

where $u_{M_2}(\boldsymbol{\mu})$ is the solution computed using $\Psi_N^{M_2}$, and $u_{M_1}(\boldsymbol{\mu})$ is the solution from $\Phi_N^{M_1}$. By substituting $u_{M_1}(\boldsymbol{\mu}) = \sum_{i=1}^{M_1} \alpha_{M_1,i} \phi_i$ and $u_{M_2}(\boldsymbol{\mu}) = \sum_{m=1}^{M_2} \beta_{M_2,m} \psi_m$ into (34), we obtain

$$\begin{aligned} \bar{\epsilon}_{M_1 M_2}^u(\boldsymbol{\mu}) &= (\|u_{M_2}(\boldsymbol{\mu})\|_X^2 + \|u_{M_1}(\boldsymbol{\mu})\|_X^2 - 2(u_{M_2}(\boldsymbol{\mu}), u_{M_1}(\boldsymbol{\mu}))_X)^{1/2} \\ &= \left((\boldsymbol{\alpha}_{M_1}(\boldsymbol{\mu}))^T \mathbf{B}_{M_1} \boldsymbol{\alpha}_{M_1}(\boldsymbol{\mu}) + (\boldsymbol{\beta}_{M_2}(\boldsymbol{\mu}))^T \mathbf{B}_{M_2} \boldsymbol{\beta}_{M_2}(\boldsymbol{\mu}) \right. \\ &\quad \left. - 2(\boldsymbol{\alpha}_{M_1}(\boldsymbol{\mu}))^T \mathbf{B}_{M_1 M_2} \boldsymbol{\beta}_{M_2}(\boldsymbol{\mu}) \right)^{1/2} \end{aligned} \quad (35)$$

where

$$B_{M_1,ij} = (\phi_i, \phi_j)_X, \quad B_{M_2,ml} = (\psi_m, \psi_l)_X, \quad B_{M_1 M_2,im} = (\phi_i, \psi_m)_X \quad (36)$$

for $1 \leq i, j \leq M_1$ and $1 \leq m, l \leq M_2$. Computing $\bar{\epsilon}_{M_1 M_2}^u(\boldsymbol{\mu})$ from (35) requires only $O(M_2^2)$ operation counts.

4.4. Offline-Online Decomposition

Offline-online decomposition is a key strategy used in RB methods to efficiently solve parametrized PDEs. This decomposition separates the computationally demanding tasks, performed during the offline stage, from the real-time, low-cost computations required during the online stage.

The offline stage of the generative RB approach is summarized in Algorithm 1. The offline stage is computationally intensive as it involves several key steps required to construct ROMs. In the offline stage, we must compute N FE solutions at selected parameter points to form the initial snapshot set. The generative snapshot method is then applied to generate additional snapshots and compress them to construct generative RB spaces. Moreover, the offline stage requires the computation of inner products to form several parameter-independent quantities. The computational complexity of the offline stage is typically dominated by the number of FE solves.

Algorithm 1 Offline stage of the generative RB approach.

Require: The parameter sample set $S_N = \{\boldsymbol{\mu}_n, 1 \leq n \leq N\}$.

Ensure: $\mathbf{l}_{M_1}, \mathbf{l}_{M_1}^O, \mathbf{A}_{M_1}^q, \mathbf{l}_{M_2}, \mathbf{l}_{M_2}^O, \mathbf{A}_{M_2}^q, \mathbf{B}_{M_1}, \mathbf{B}_{M_2}, \mathbf{B}_{M_1M_2}$.

- 1: Solve the FE formulation (22) for each $\boldsymbol{\mu}_n \in S_N$ to obtain $\{u(\boldsymbol{\mu}_n)\}_{n=1}^N$.
 - 2: Construct the generative RB spaces defined in (25) using the generative snapshot method.
 - 3: Compute and store $\mathbf{l}_{M_1}, \mathbf{l}_{M_1}^O, \mathbf{A}_{M_1}^q$ from (29), and $\mathbf{l}_{M_2}, \mathbf{l}_{M_2}^O, \mathbf{A}_{M_2}^q$ from (32).
 - 4: Compute and store $\mathbf{B}_{M_1}, \mathbf{B}_{M_2}, \mathbf{B}_{M_1M_2}$ from (36).
-

The online stage of the generative RB approach is summarized in Algorithm 2. The online stage computes the RB output $s_{M_1}(\boldsymbol{\mu})$, and the error estimates $\bar{\epsilon}_{M_1M_2}^s(\boldsymbol{\mu})$ and $\bar{\epsilon}_{M_1M_2}^u(\boldsymbol{\mu})$ for any given input $\boldsymbol{\mu} \in \mathcal{D}$. The computational complexity to evaluate the RB output is $O(QM_1^2 + M_1^3)$. On the other hand, the computational complexity to evaluate error estimates is $O(QM_2^2 + M_2^3)$. Since $M_2 > M_1$, the overall computational complexity is $O(QM_2^2 + M_2^3)$. The computational cost of the online stage of the generative RB approach is higher than that of the standard RB approach, which is $O(QN^2 + N^3)$. Despite the higher complexity, the larger RB spaces and the error estimates ensure improved accuracy and reliability of the RB approximation, which justify the increased computational cost.

Algorithm 2 Online stage of the generative RB approach.

Require: Parameter point $\boldsymbol{\mu} \in \mathcal{D}$.

Ensure: RB output $s_{M_1}(\boldsymbol{\mu})$, error estimates $\bar{\epsilon}_{M_1 M_2}^s(\boldsymbol{\mu})$ and $\bar{\epsilon}_{M_1 M_2}^u(\boldsymbol{\mu})$.

- 1: Form the RB system (28) with $O(QM_1^2)$ operation counts.
 - 2: Solve the RB system (28) for $\boldsymbol{\alpha}_{M_1}(\boldsymbol{\mu})$ and calculate $s_{M_1}(\boldsymbol{\mu})$ from (27), which costs $O(M_1^3)$ operation counts.
 - 3: Form the RB system (31) with $O(QM_2^2)$ operation counts.
 - 4: Solve the RB system (31) for $\boldsymbol{\beta}_{M_2}(\boldsymbol{\mu})$ and calculate $s_{M_2}(\boldsymbol{\mu})$ from (30), which costs $O(M_2^3)$ operation counts.
 - 5: Compute $\bar{\epsilon}_{M_1 M_2}^s(\boldsymbol{\mu})$ from (33) and $\bar{\epsilon}_{M_1 M_2}^u(\boldsymbol{\mu})$ from (35), which costs $O(M_2^2)$ operation counts.
-

4.5. Greedy Sampling Algorithm

The greedy sampling algorithm is an iterative procedure employed in RB methods to select a set of parameter points from the parameter space that maximizes the accuracy of the ROM. The greedy algorithm constructs a reduced basis with the minimal number of basis functions required to achieve a desired level of accuracy. The greedy algorithm leverages the offline-online decomposition to efficiently construct the ROM during the offline phase and evaluate it during the online phase. The algorithm relies on inexpensive and tight *a posteriori* error estimates to explore the parameter space effectively without requiring a large number of FOM solves. The greedy algorithm of the generative RB approach is summarized in Algorithm 3.

Algorithm 3 Greedy sampling of the generative RB approach.

Require: The initial parameter sample $S_N = \{\boldsymbol{\mu}_n\}_{n=1}^N$, the training set $\Xi_K^{\text{train}} = \{\boldsymbol{\mu}_k^{\text{train}}\}_{k=1}^K$, and error tolerance ϵ_{tol} .

Ensure: $\boldsymbol{l}_{M_1}, \boldsymbol{l}_{M_1}^O, \boldsymbol{A}_{M_1}^q, \boldsymbol{l}_{M_2}, \boldsymbol{l}_{M_2}^O, \boldsymbol{A}_{M_2}^q, \boldsymbol{B}_{M_1}, \boldsymbol{B}_{M_2}, \boldsymbol{B}_{M_1 M_2}$.

- 1: Perform Algorithm 1 to form and store $\boldsymbol{l}_{M_1}, \boldsymbol{l}_{M_1}^O, \boldsymbol{A}_{M_1}^q, \boldsymbol{l}_{M_2}, \boldsymbol{l}_{M_2}^O, \boldsymbol{A}_{M_2}^q, \boldsymbol{B}_{M_1}, \boldsymbol{B}_{M_2}, \boldsymbol{B}_{M_1 M_2}$.
 - 2: Perform Algorithm 2 to calculate $\bar{\epsilon}_{M_1 M_2}^s(\boldsymbol{\mu}_k^{\text{train}}), 1 \leq k \leq K$.
 - 3: Find the next parameter point as $\boldsymbol{\mu}_{N+1} = \arg \max_{1 \leq k \leq K} \bar{\epsilon}_{M_1 M_2}^s(\boldsymbol{\mu}_k^{\text{train}})$.
 - 4: If $\bar{\epsilon}_{M_1 M_2}^s(\boldsymbol{\mu}_{N+1}) \leq \epsilon_{\text{tol}}$ then stop. Otherwise update the parameter sample $S_N = S_N \cup \boldsymbol{\mu}_{N+1}$ and go back to Step 1.
-

5. Numerical results

In this section, we present numerical results from two affine linear PDEs to demonstrate the generative RB method and compare its performance to that of the standard RB method. To this end, we introduce the following maximum relative errors

$$\epsilon_{\max, \text{rel}}^u = \max_{\boldsymbol{\mu} \in \Xi^{\text{test}}} \frac{\epsilon_{M_1}^u(\boldsymbol{\mu})}{\|u(\boldsymbol{\mu})\|_X}, \quad \epsilon_{\max, \text{rel}}^s = \max_{\boldsymbol{\mu} \in \Xi^{\text{test}}} \frac{\epsilon_{M_1}^s(\boldsymbol{\mu})}{|s(\boldsymbol{\mu})|} \quad (37)$$

and their estimates as

$$\bar{\epsilon}_{\max, \text{rel}}^u = \max_{\boldsymbol{\mu} \in \Xi^{\text{test}}} \frac{\bar{\epsilon}_{M_1, M_2}^u(\boldsymbol{\mu})}{\|u_{M_2}(\boldsymbol{\mu})\|_X}, \quad \bar{\epsilon}_{\max, \text{rel}}^s = \max_{\boldsymbol{\mu} \in \Xi^{\text{test}}} \frac{\bar{\epsilon}_{M_1, M_2}^s(\boldsymbol{\mu})}{|s_{M_2}(\boldsymbol{\mu})|}, \quad (38)$$

where Ξ^{test} is a test sample of N^{test} parameter points distributed uniformly in the parameter domain. Similarly, the mean relative errors, $\epsilon_{\text{mean,rel}}^u$ and $\epsilon_{\text{mean,rel}}^s$, and their estimates, $\bar{\epsilon}_{\text{mean,rel}}^u$ and $\bar{\epsilon}_{\text{mean,rel}}^s$, are defined.

5.1. Convection-Diffusion Problem

We consider a linear convection-diffusion problem

$$-\nabla^2 u^e + \nabla \cdot (\boldsymbol{\mu} u^e) = 100, \quad \text{in } \Omega, \quad (39)$$

with homogeneous Dirichlet condition $u^e = 0$ on $\partial\Omega$. Here $\Omega = (0, 1)^2$ is a unit square domain, while $\boldsymbol{\mu} = (\mu_1, \mu_2)$ is the parameter vector in a parameter domain $\mathcal{D} \equiv [0, 50] \times [0, 50]$. Let $X \in H_0^1(\Omega)$ be a finite element (FE) approximation space of dimension \mathcal{N} with $X = \{v \in H_0^1(\Omega) : v|_K \in \mathcal{P}^3(T), \forall T \in \mathcal{T}_h\}$, where $\mathcal{P}^3(T)$ is a space of polynomials of degree 3 on an element $T \in \mathcal{T}_h$ and \mathcal{T}_h is a finite element grid of 32×32 quadrilaterals. The dimension of the FE space X is $\mathcal{N} = 9409$. The FE approximation $u(\boldsymbol{\mu}) \in X$ of the exact solution $u^e(\boldsymbol{\mu})$ is the solution of

$$\int_{\Omega} \nabla u \cdot \nabla v - \int_{\Omega} \boldsymbol{\mu} u \cdot \nabla v = 100 \int_{\Omega} v, \quad \forall v \in X. \quad (40)$$

The output of interest is evaluated as $s(\boldsymbol{\mu}) = \ell^O(u(\boldsymbol{\mu}))$ with $\ell^O(v) \equiv \int_{\Omega} v$.

Figure 8 shows the selected parameter points and the maximum relative error estimate as a function of N . The plot reveals that the majority of the points are concentrated along the boundary of the parameter domain. This distribution suggests that the regions near the boundary exhibit greater

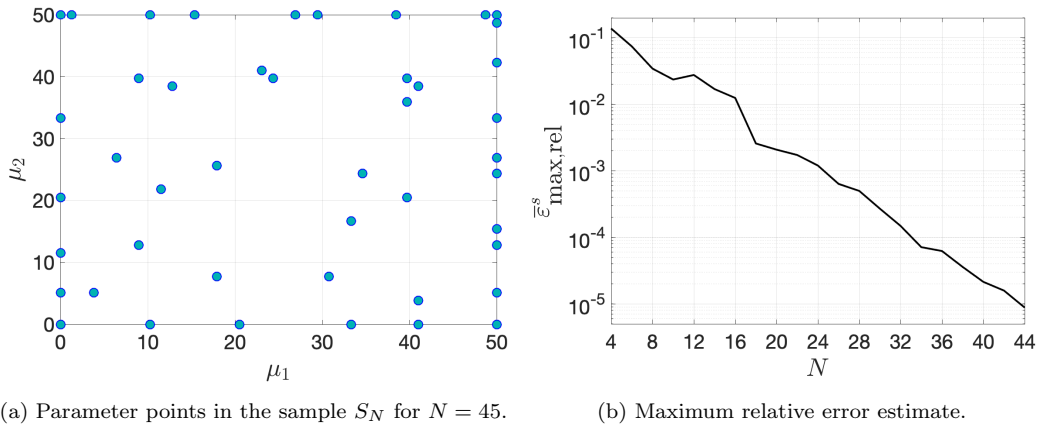


Figure 8: Greedy sampling algorithm results: (a) distribution of the parameter sample points selected from a grid of 40×40 uniformly distributed points in the parameter domain, and (b) the convergence of the maximum relative error estimate for the RB output.

variability or complexity in the solution manifold, requiring more refined sampling. The greedy algorithm terminates at $N = 45$, where the maximum relative error estimate is less than 10^{-5} .

Figure 9 presents the maximum relative errors, $\epsilon_{\max, \text{rel}}^u$ and $\epsilon_{\max, \text{rel}}^s$, as a function of N for both the standard RB method and the generative RB method. The test set Ξ^{test} is a uniform grid of $N^{\text{test}} = 30 \times 30$ points in the parameter domain. The generative RB method consistently shows lower errors compared to the standard RB method across all three activation functions considered. Among these, the softplus and exponential functions exhibit similar convergence behaviors, while the quadratic function achieves the fastest convergence rate and the smallest errors, particularly for larger values of N . In particular, at $N = 45$, the generative RB method with $M_1 = 3N$ produces output errors that are approximately 1000 times smaller than those of the standard RB method.

Figure 10 shows the mean relative errors, $\epsilon_{\text{mean,rel}}^u$ and $\epsilon_{\text{mean,rel}}^s$, together with their error estimates, $\bar{\epsilon}_{\text{mean,rel}}^u$ and $\bar{\epsilon}_{\text{mean,rel}}^s$, as functions of N . The error estimates are calculated using $M_2 = M_1 + N$. The error estimates closely match the true errors, indicating that the error estimates are very tight and provide a reliable measure of accuracy. Although error estimates are not provably rigorous – evident in cases where they are slightly smaller than true errors – their tightness serves as a strong indicator of the accuracy and reliability of the generative RB method. This tight correlation between

estimated and true errors reinforces the efficacy of the generative RB method.

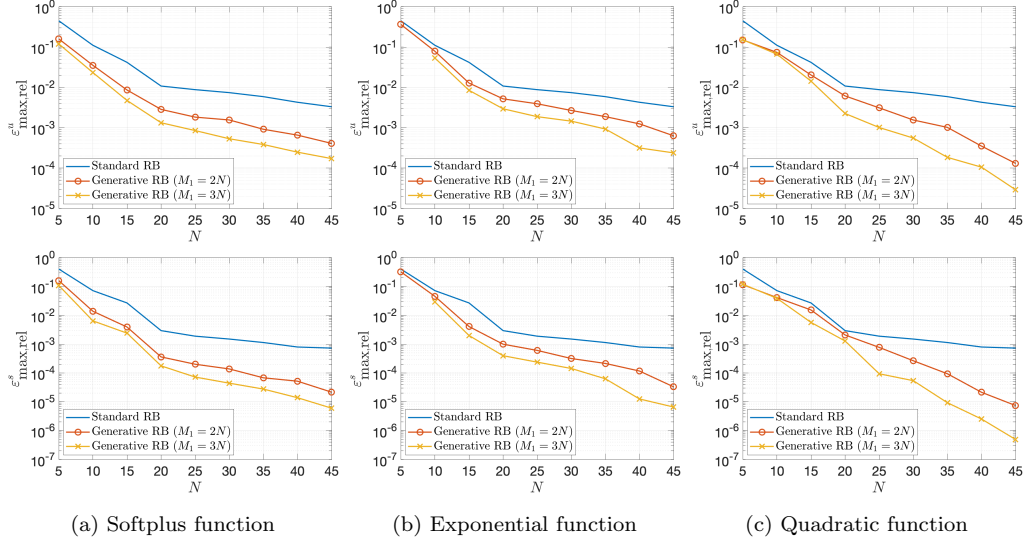


Figure 9: Convergence of the maximum relative error in the RB solution (top) and in the RB output (bottom) as a function of N .

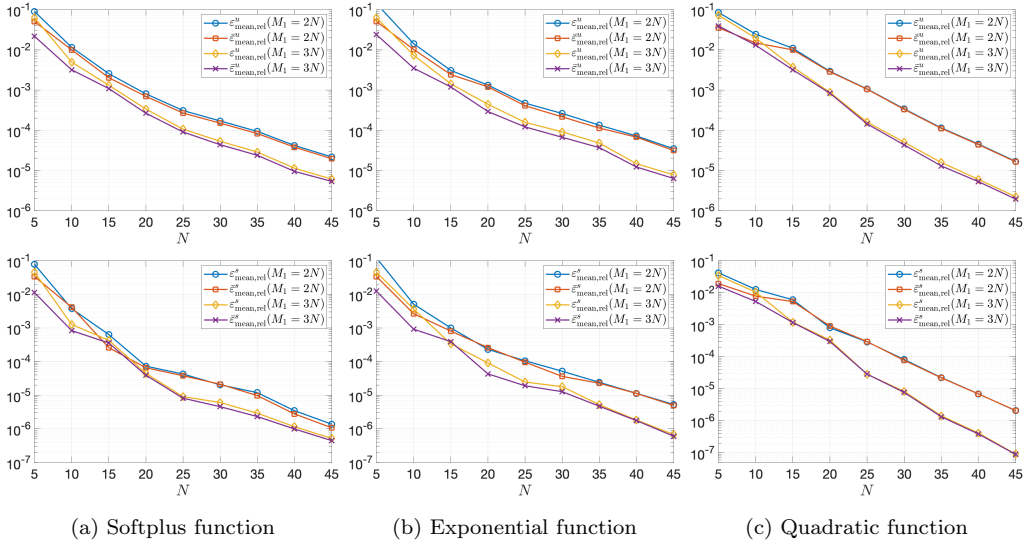


Figure 10: Convergence of the mean relative error and the mean error estimate in the RB solution (top) and in the RB output (bottom) as a function of N . The error estimates are calculated using $M_2 = M_1 + N$.

5.2. Reaction-Diffusion Problem

We consider a linear reaction-diffusion problem

$$-\nabla \cdot (\kappa(\mathbf{x}, \boldsymbol{\mu}) \nabla u) + u = 0 \quad \text{in } \Omega, \quad (41)$$

with Dirichlet and Neumann boundary conditions

$$u = 0 \quad \text{on } \Gamma_2, \quad \kappa(\mathbf{x}, \boldsymbol{\mu}) \nabla u \cdot \mathbf{n} = 1 \quad \text{on } \Gamma_1, \quad (42)$$

and Robin boundary conditions

$$\kappa(\mathbf{x}, \boldsymbol{\mu}) \nabla u \cdot \mathbf{n} + \mu_3 u = 0 \quad \text{on } \Gamma_3, \quad \kappa(\mathbf{x}, \boldsymbol{\mu}) \nabla u \cdot \mathbf{n} + \mu_4 u = 0 \quad \text{on } \Gamma_4. \quad (43)$$

Here $\Omega = \Omega_1 \cup \Omega_2$ is the T -shaped domain as shown in Figure 11(a). Γ_1 is the bottom boundary and Γ_2 is the top boundary, while Γ_3 and Γ_4 are the remaining part of the boundary of Ω_1 and Ω_2 , respectively. The thermal conductivity has the form

$$\kappa(\mathbf{x}, \boldsymbol{\mu}) = \begin{cases} \mu_1, & \mathbf{x} \in \Omega_1, \\ \mu_2, & \mathbf{x} \in \Omega_2. \end{cases} \quad (44)$$

The parameter domain is $\mathcal{D} \equiv [1, 10] \times [1, 10] \times [0, 10] \times [0, 10]$. The output of interest is the average of the field variable over the physical domain. For any given $\boldsymbol{\mu} \in \mathcal{D}$, we evaluate $s(\boldsymbol{\mu}) = \int_{\Omega} u(\boldsymbol{\mu})$, where $u(\boldsymbol{\mu}) \in X \subset H_0^1(\Omega) \equiv \{v \in H^1(\Omega) \mid v|_{\Gamma_1} = 0\}$ is the solution of

$$\mu_1 \int_{\Omega_1} \nabla u \cdot \nabla v + \mu_2 \int_{\Omega_2} \nabla u \cdot \nabla v + \mu_3 \int_{\Gamma_3} uv + \mu_4 \int_{\Gamma_4} uv + \int_{\Omega} uv = \int_{\Gamma_2} v, \quad \forall v \in X.$$

The FE approximation space is $X = \{v \in H_0^1(\Omega) : v|_K \in \mathcal{P}^3(T), \forall T \in \mathcal{T}_h\}$, where $\mathcal{P}^3(T)$ is a space of polynomials of degree 3 on an element $T \in \mathcal{T}_h$ and \mathcal{T}_h is a mesh of 900 quadrilaterals. The dimension of X is $\mathcal{N} = 8401$. Figure 11 shows FE solutions at two different parameter points.

Table 2 shows the parameter points and the maximum relative error estimate as a function of N during the greedy cycle. The first four parameter points form the initial parameter set S_N . The greedy sampling is applied to a grid of $8 \times 8 \times 8 \times 8$ uniformly distributed parameter points and terminated at $N = 20$, where the maximum relative error estimate is less than 10^{-5} . The error estimates are calculated using $M_1 = 2N$ and $M_2 = 4N$. All selected parameter points are on the boundary of the parameter domain, suggesting

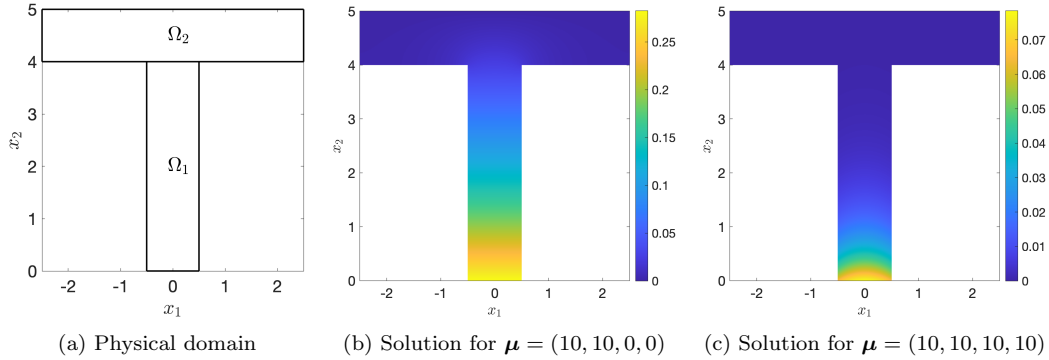


Figure 11: Physical domain and FE solutions at two parameter points for the linear reaction-diffusion problem.

N	μ_1	μ_2	μ_3	μ_4	$\bar{\epsilon}_{\max, \text{rel}}^s$
1	1	1	0	0	—
2	10	10	10	10	—
3	10	1	0	10	—
4	1	10	10	0	—
5	10	10	0	0	1.06E-01
6	10	1	0	0	6.99E-02
7	3.5714	1	10	10	5.43E-03
8	10	1	5.7143	0	5.61E-03
9	1	1	5.7143	10	2.03E-03
10	10	3.5714	0	0	1.01E-03
11	10	1	1.4286	0	1.13E-03
12	10	1	0	2.8571	8.77E-04
13	10	4.8571	0	4.2857	3.59E-04
14	6.1429	2.2857	0	10	1.78E-04
15	3.5714	1	0	10	7.66E-05
16	10	1	10	0	3.96E-05
17	1	1	1.4286	7.1429	2.79E-05
18	10	6.1429	2.8571	0	1.61E-05
19	3.5714	10	0	0	1.62E-05
20	10	1	0	7.1429	3.34E-06

Table 2: Selected parameter points and the maximum relative errors during the greedy sampling cycle for the heat conduction problem. The greedy algorithm is applied to a grid of $8 \times 8 \times 8 \times 8$ uniformly distributed points in the parameter domain.

that the regions near the boundary exhibit greater variability or complexity in the solution manifold.

Figure 12 presents the maximum relative errors, $\epsilon_{\max, \text{rel}}^u$ and $\epsilon_{\max, \text{rel}}^s$, as

a function of N for both the standard RB method and the generative RB method. The test set Ξ^{test} is a uniform grid of $N^{\text{test}} = 6 \times 6 \times 6 \times 6$ points in the parameter domain. The generative RB method consistently shows lower errors compared to the standard RB method for the softplus and exponential functions. The softplus and exponential functions exhibit similar convergence behaviors. For the exponential function with $N = 20$ and $M_1 = 60$, the generative RB method produces output errors that are approximately 100 times smaller than those of the standard RB method. Unlike the previous example, the quadratic function performs poorly in this example.

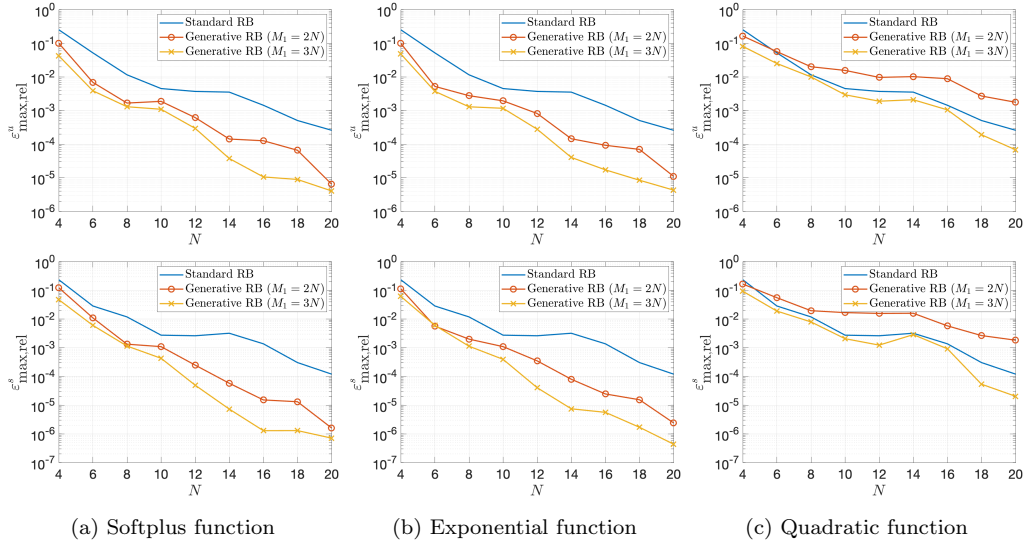


Figure 12: Convergence of the maximum relative error in the RB solution (top) and in the RB output (bottom) as a function of N .

Figure 13 shows the mean relative errors, $\epsilon_{\text{mean,rel}}^u$ and $\epsilon_{\text{mean,rel}}^s$, together with their error estimates, $\bar{\epsilon}_{\text{mean,rel}}^u$ and $\bar{\epsilon}_{\text{mean,rel}}^s$, as functions of N . The error estimates are calculated using $M_2 = M_1 + N$. The error estimates closely match the true errors and thus provide a reliable measure of accuracy. These results highlight the importance of selecting an appropriate activation function and demonstrate the potential of the generative RB method for achieving high accuracy for problems in high-dimensional parameter spaces.

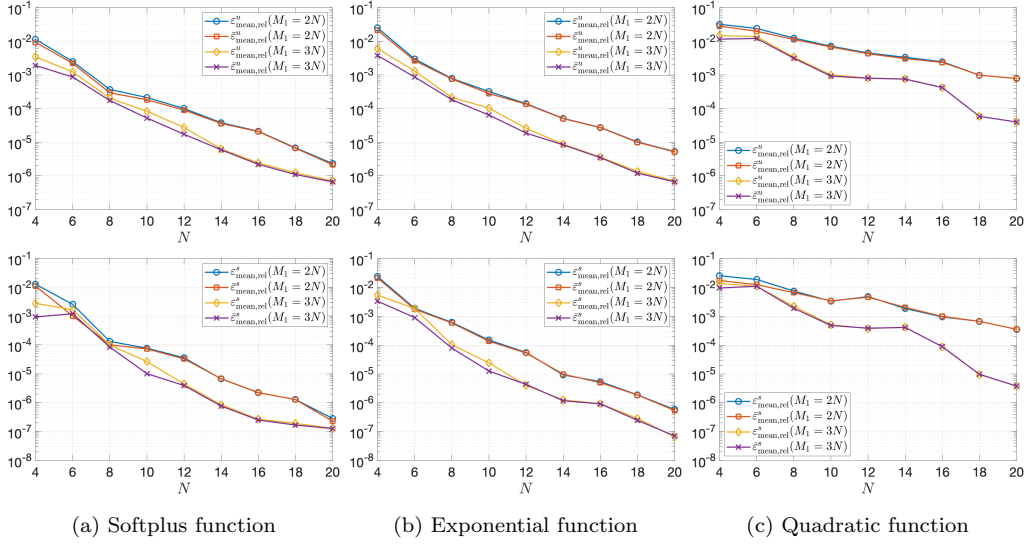


Figure 13: Convergence of the mean relative error and the mean error estimate in the RB solution (top) and in the RB output (bottom) as a function of N . The error estimates are calculated by using $M_2 = M_1 + N$.

6. Conclusion

In this paper, we introduced generative reduced basis (RB) methods to construct reduced-order models (ROMs) for parametrized partial differential equations. While the generative RB methods have demonstrated significant advantages compared to the standard RB method, there are several avenues for future work to further advance the approach.

Given that the choice of nonlinear activation function plays a critical role in the performance of the generative RB method, it becomes evident that optimizing the activation function is paramount for achieving optimal accuracy and efficiency. Future work should focus on developing systematic procedures to identify the most suitable activation function for a given problem. This could involve adaptive learning techniques that adjust the activation function based on error metrics, parameter space exploration, or the use of optimization algorithms to tailor the activation function to the specific characteristics of the solution manifold. Such an approach would further enhance the generative RB method and make it even more effective for a wider range of complex high-dimensional problems.

One key area for future research is the extension of generative RB methods

to non-affine and nonlinear problems, where traditional linear approximation techniques face greater challenges. Developing robust strategies to handle such complexities will broaden the applicability of generative RB methods to a wider range of physical and engineering problems.

Another direction is the integration of adaptive strategies within the generative framework. An adaptive refinement process could dynamically adjust the number and distribution of snapshots, further optimizing the construction of RB spaces based on the problem’s specific characteristics. This would enable more efficient ROMs, especially for problems where solution behavior varies significantly across the parameter space.

Additionally, machine learning techniques could be incorporated to enhance the scalability and generalization capabilities of generative RB methods. For example, data-driven ROMs could be trained on smaller sets of solution snapshots by using the generative snapshot method. This would significantly reduce the offline computational cost and improve the overall efficiency of the method.

Lastly, there is potential for developing nonlinear manifold methods that go beyond linear approximation spaces. These methods could allow for the efficient approximation of the solution manifold by using nonlinear embeddings, particularly in cases where traditional RB methods exhibit slow convergence due to highly nonlinear features. However, a challenge associated with nonlinear manifold methods is the requirement for extensive snapshot sets to train the nonlinear mappings effectively. The generative snapshot method can be used to enrich the snapshot set and thus enhance the efficiency and accuracy of nonlinear manifold methods.

Acknowledgements

I would like to thank Professors Jaime Peraire, Anthony T. Patera, and Robert M. Freund at MIT for fruitful discussions. I gratefully acknowledge a Seed Grant from the MIT Portugal Program, the United States Department of Energy under contract DE-NA0003965, the National Science Foundation under grant number NSF-PHY-2028125, and the Air Force Office of Scientific Research under Grant No. FA9550-22-1-0356 for supporting this work.

References

- [1] Y. Chen, J. S. Hesthaven, Y. Maday, J. Rodríguez, Improved successive constraint method based a posteriori error estimate for re-

- duced basis approximation of 2D Maxwell's problem, *ESAIM - Mathematical Modelling and Numerical Analysis* 43 (6) (2009) 1099–1116. doi:10.1051/m2an/2009037.
- [2] Y. Chen, J. S. Hesthaven, Y. Maday, J. Rodríguez, Certified Reduced Basis Methods and Output Bounds for the Harmonic Maxwell's Equations, *SIAM Journal on Scientific Computing* 32 (2) (2010) 970–996. doi:10.1137/09075250X.
URL <http://epubs.siam.org/action/showAbstract?page=970&volume=32&issue=2&journalCode=sjoc3>
- [3] S. Deparis, Reduced basis error bound computation of parameter-dependent Navier-stokes equations by the natural norm approach, *SIAM Journal on Numerical Analysis* 46 (4) (2008) 2039–2067. doi:10.1137/060674181.
- [4] J. Eftang, A. Patera, E. Ronquist, An "hp" Certified Reduced Basis Method for Parametrized Elliptic Partial Differential Equations, *SIAM Journal on Scientific Computing* 32 (6) (2010) 3170–3200.
- [5] J. L. Eftang, D. B. Huynh, D. J. Knezevic, A. T. Patera, A two-step certified reduced basis method, *Journal of Scientific Computing* 51 (1) (2012) 28–58. doi:10.1007/s10915-011-9494-2.
- [6] D. B. Huynh, A. T. Patera, Reduced basis approximation and a posteriori error estimation for stress intensity factors, *International Journal for Numerical Methods in Engineering* 72 (10) (2007) 1219–1259. doi:10.1002/nme.2090.
- [7] D. Huynh, D. Knezevic, Y. Chen, J. Hesthaven, A. Patera, A natural-norm Successive Constraint Method for inf-sup lower bounds, *Computer Methods in Applied Mechanics and Engineering* 199 (29-32) (2010) 1963–1975. doi:10.1016/j.cma.2010.02.011.
URL <http://dx.doi.org/10.1016/j.cma.2010.02.011>
- [8] D. B. P. Huynh, D. J. Knezevic, A. T. Patera, A Static condensation Reduced Basis Element method : Approximation and a posteriori error estimation, *Mathematical Modelling and Numerical Analysis* 47 (1) (2013) 213–251. doi:10.1051/m2an/2012022.

- [9] M. Kärcher, Z. Tokoutsi, M. A. Grepl, K. Veroy, Certified Reduced Basis Methods for Parametrized Elliptic Optimal Control Problems with Distributed Controls, *Journal of Scientific Computing* 75 (1) (2018) 276–307. doi:10.1007/s10915-017-0539-z.
- [10] D. J. Knezevic, N. C. Nguyen, A. T. Patera, Reduced basis approximation and a posteriori error estimation for the parametrized unsteady Boussinesq equations, *Mathematical Models and Methods in Applied Sciences* 21 (7) (2011) 1415–1442. doi:10.1142/S0218202511005441.
- [11] D. J. Knezevic, A. T. Patera, A certified reduced basis method for the fokker-planck equation of dilute polymeric fluids: Fene dumbbells in extensional flow, *SIAM Journal on Scientific Computing* 32 (2) (2010) 793–817. doi:10.1137/090759239.
- [12] N. C. Nguyen, K. Veroy, A. T. Patera, Certified Real-Time Solution of Parametrized Partial Differential Equations, in: S. Yip (Ed.), *Handbook of Materials Modeling*, Kluwer Academic Publishing, 2004, pp. 1523–1559.
- [13] N. C. Nguyen, A posteriori error estimation and basis adaptivity for reduced-basis approximation of nonaffine-parametrized linear elliptic partial differential equations, *Journal of Computational Physics* 227 (2) (2007) 983–1006. doi:10.1016/j.jcp.2007.08.031.
URL <http://linkinghub.elsevier.com/retrieve/pii/S0021999107003749>
- [14] N. C. Nguyen, G. Rozza, D. B. P. Huynh, A. T. Patera, Reduced Basis Approximation and A Posteriori Error Estimation for Parametrized Parabolic PDEs; Application to Real-Time Bayesian Parameter Estimation, in: Biegler, Biros, Ghattas, Heinkenschloss, Keyes, Mallick, Tenorio, van Bloemen Waanders, Willcox (Eds.), *Computational Methods for Large Scale Inverse Problems and Uncertainty Quantification*, John Wiley and Sons, UK, 2010.
- [15] N. C. Nguyen, G. Rozza, A. T. Patera, Reduced basis approximation and a posteriori error estimation for the time-dependent viscous Burgers’ equation, *Calcolo* 46 (3) (2009) 157–185. doi:10.1007/s10092-009-0005-x.
URL <http://link.springer.com/10.1007/s10092-009-0005-x>

- [16] G. Rozza, D. B. P. Huynh, A. T. Patera, Reduced basis approximation and a posteriori error estimation for affinely parametrized elliptic coercive partial differential equations: Application to transport and continuum mechanics, *Archives Computational Methods in Engineering* 15 (3) (2008) 229–275. doi:10.1007/s11831-008-9019-9.
URL <http://link.springer.com/10.1007/s11831-008-9019-9>
- [17] G. Rozza, Reduced-basis methods for elliptic equations in sub-domains with $\{ \backslash \em a \text{ posteriori} \backslash / \}$ error bounds and adaptivity, *Appl. Numer. Math.* 55 (4) (2005) 403–424.
- [18] S. Sen, K. Veroy, D. B. Huynh, S. Deparis, N. C. Nguyen, A. T. Patera, "Natural norm" a posteriori error estimators for reduced basis approximations, *Journal of Computational Physics* 217 (1) (2006) 37–62. doi:10.1016/j.jcp.2006.02.012.
- [19] K. Veroy, A. T. Patera, Certified real-time solution of the parametrized steady incompressible Navier-Stokes equations: Rigorous reduced-basis a posteriori error bounds, *International Journal for Numerical Methods in Fluids* 47 (8-9) (2005) 773–788. doi:10.1002/flid.867.
- [20] K. Veroy, D. V. Rovas, A. T. Patera, A posteriori error estimation for reduced-basis approximation of parametrized elliptic coercive partial differential equations: "Convex inverse" bound conditioners, *ESAIM - Control, Optimisation and Calculus of Variations* 8 (2002) 1007–1028. doi:10.1051/cocv:2002041.
- [21] F. Vidal-Codina, N. C. Nguyen, M. B. Giles, J. Peraire, A model and variance reduction method for computing statistical outputs of stochastic elliptic partial differential equations, *Journal of Computational Physics* 297 (2015) 700–720. arXiv:1409.1526, doi:10.1016/j.jcp.2015.05.041.
- [22] F. Vidal-Codina, N. C. Nguyen, J. Peraire, Computing parametrized solutions for plasmonic nanogap structures, *Journal of Computational Physics* 366 (2018) 89–106. arXiv:1710.06539, doi:10.1016/j.jcp.2018.04.009.
- [23] Y. Maday, N. C. Nguyen, A. T. Patera, S. Pau, G. S. H. Pau, A general, multipurpose interpolation procedure: the magic points.,

- Communications on Pure and Applied Analysis 8 (1) (2009) 383–404.
doi:10.3934/cpaa.2009.8.383.
URL <http://www.aims sciences.org/journals/displayArticles.jsp?paperID=3753>
- [24] L. Sirovich, Turbulence and the Dynamics of Coherent Structures, Part 1: Coherent Structures, Quarterly of Applied Mathematics 45 (3) (1987) 561–571.
- [25] K. Kunisch, S. Volkwein, Galerkin proper orthogonal decomposition methods for parabolic problems, Numerische Mathematik 148 (2001) 117–148.
URL <http://link.springer.com/article/10.1007/s002110100282>
- [26] N. C. Nguyen, A. T. Patera, J. Peraire, A 'best points' interpolation method for efficient approximation of parametrized functions, International Journal for Numerical Methods in Engineering 73 (4) (2008) 521–543. doi:10.1002/nme.2086.
URL <http://doi.wiley.com/10.1002/nme.2086>
- [27] T. Bui-Thanh, K. Willcox, O. Ghattas, Model Reduction for Large-Scale Systems with High-Dimensional Parametric Input Space, Proceedings of the 48th AIAA/ASME/ASCE/AHS/ASC Structures, Structural Dynamics and Material Conference 30 (6) (2008) 3270–3288.
- [28] A. Buffa, Y. Maday, A. T. Patera, C. Prud'homme, G. Turinici, A priori convergence of the Greedy algorithm for the parametrized reduced basis method, ESAIM: Mathematical Modelling and Numerical Analysis 46 (03) (2012) 595–603. doi:10.1051/m2an/2011056.
URL http://journals.cambridge.org/abstract/_S0764583X11000562%}5Cnhttp://www.esaim-m2an.org/10.1051/m2an/2011056
- [29] T. Bui-Thanh, K. Willcox, O. Ghattas, B. van Bloemen Waanders, Goal-oriented, model-constrained optimization for reduction of large-scale systems, Journal of Computational Physics 224 (2) (2007) 880–896. doi:10.1016/j.jcp.2006.10.026.
- [30] J. S. Hesthaven, B. Stamm, S. Zhang, Efficient greedy algorithms for high-dimensional parameter spaces with applications to empirical interpolation and reduced basis methods, ESAIM: Mathematical Modelling

- and Numerical Analysis 48 (1) (2014) 259–283. doi:10.1051/m2an/2013100.
- [31] R. DeVore, G. Petrova, P. Wojtaszczyk, Greedy Algorithms for Reduced Bases in Banach Spaces, *Constructive Approximation* 37 (3) (2013) 455–466. arXiv:1204.2290, doi:10.1007/s00365-013-9186-2.
- [32] B. Haasdonk, Convergence rates of the pod—greedy method, *Mathematical Modelling and Numerical Analysis* 47 (3) (2013) 859–873. doi:10.1051/m2an/2012045.
- [33] K. Hoang, B. Khoo, G. Liu, N. Nguyen, A. Patera, Rapid identification of material properties of the interface tissue in dental implant systems using reduced basis method, *Inverse Problems in Science and Engineering* 21 (8) (2013) 1310–1334. doi:10.1080/17415977.2012.757315. URL <http://dx.doi.org/10.1080/17415977.2012.757315>
- [34] P. Binev, A. Cohen, W. Dahmen, R. DeVore, G. Petrova, P. Wojtaszczyk, Convergence rates for greedy algorithms in reduced basis methods, *SIAM Journal on Mathematical Analysis* 43 (3) (2011) 1457–1472. doi:10.1137/100795772.
- [35] N. C. Nguyen, J. Peraire, Gaussian functional regression for output prediction: Model assimilation and experimental design, *Journal of Computational Physics* 309 (2016) 52–68. doi:10.1016/J.JCP.2015.12.035. URL <https://www.sciencedirect.com/science/article/pii/S0021999115008542>
- [36] C. Lieberman, K. Willcox, O. Ghattas, Parameter and state model reduction for large-scale statistical inverse problems, *SIAM Journal on Scientific Computing* 32 (5) (2010) 2523–2542. doi:10.1137/090775622.
- [37] B. Haasdonk, M. Dihlmann, M. Ohlberger, A training set and multiple bases generation approach for parameterized model reduction based on adaptive grids in parameter space, *Mathematical and Computer Modelling of Dynamical Systems* 17 (4) (2011) 423–442. doi:10.1080/13873954.2011.547674.
- [38] M. Hess, A. Alla, A. Quaini, G. Rozza, M. Gunzburger, A localized reduced-order modeling approach for PDEs with bifurcating solutions,

- Computer Methods in Applied Mechanics and Engineering 351 (2019) 379–403. [arXiv:1807.08851](https://arxiv.org/abs/1807.08851), [doi:10.1016/j.cma.2019.03.050](https://doi.org/10.1016/j.cma.2019.03.050).
- [39] Y. Maday, B. Stamm, Locally adaptive greedy approximations for anisotropic parameter reduced basis spaces, *SIAM Journal on Scientific Computing* 35 (6) (2013). [arXiv:1204.3846](https://arxiv.org/abs/1204.3846), [doi:10.1137/120873868](https://doi.org/10.1137/120873868).
- [40] J. S. Hesthaven, C. Pagliantini, N. Ripamonti, Rank-adaptive structure-preserving model order reduction of Hamiltonian systems, *ESAIM: Mathematical Modelling and Numerical Analysis* 56 (2) (2022) 617–650. [doi:10.1051/m2an/2022013](https://doi.org/10.1051/m2an/2022013).
- [41] B. Peherstorfer, K. Willcox, Dynamic data-driven reduced-order models, *Computer Methods in Applied Mechanics and Engineering* 291 (2015) 21–41. [doi:10.1016/j.cma.2015.03.018](https://doi.org/10.1016/j.cma.2015.03.018).
- [42] B. Peherstorfer, K. Willcox, Online adaptive model reduction for nonlinear systems via low-rank updates, *SIAM Journal on Scientific Computing* 37 (4) (2015) A2123–A2150. [doi:10.1137/140989169](https://doi.org/10.1137/140989169).
- [43] T. P. Sapsis, P. F. Lermusiaux, Dynamically orthogonal field equations for continuous stochastic dynamical systems, *Physica D: Nonlinear Phenomena* 238 (23-24) (2009) 2347–2360. [doi:10.1016/j.physd.2009.09.017](https://doi.org/10.1016/j.physd.2009.09.017).
- [44] R. Zimmermann, B. Peherstorfer, K. Willcox, Geometric subspace updates with applications to online adaptive nonlinear model reduction, *SIAM Journal on Matrix Analysis and Applications* 39 (1) (2018) 234–261. [doi:10.1137/17M1123286](https://doi.org/10.1137/17M1123286).
- [45] S. Boyaval, Reduced-Basis Approach for Homogenization beyond the Periodic Setting, *SIAM Multiscale Modeling & Simulation* 7 (1) (2008) 466–494.
- [46] N. C. Nguyen, A multiscale reduced-basis method for parametrized elliptic partial differential equations with multiple scales, *Journal of Computational Physics* 227 (23) (2008) 9807–9822.
 URL <http://www.scopus.com/inward/record.url?eid=2-s2.0-53349103005&partnerID=40&md5=64852a2fac4b34c956379f980e2cf264>

- [47] J. L. Eftang, A. T. Patera, Port reduction in parametrized component static condensation: Approximation and a posteriori error estimation, *International Journal for Numerical Methods in Engineering* 96 (5) (2013) 269–302. doi:10.1002/nme.4543.
- [48] K. Smetana, A new certification framework for the port reduced static condensation reduced basis element method, *Computer Methods in Applied Mechanics and Engineering* 283 (2015) 352–383. doi:10.1016/j.cma.2014.09.020.
- [49] S. Boyaval, C. L. Bris, T. Lelièvre, Y. Maday, N. C. Nguyen, A. T. Patera, C. Le Bris, T. Lelièvre, Y. Maday, N. C. Nguyen, A. T. Patera, Reduced basis techniques for stochastic problems, *Archives of Computational Methods in Engineering* 17 (4) (2010) 435–454. arXiv:1004.0357, doi:10.1007/s11831-010-9056-z.
URL <http://link.springer.com/10.1007/s11831-010-9056-z>
- [50] S. Boyaval, C. L. Bris, Y. Maday, N. C. Nguyen, A. T. Patera, A reduced basis approach for variational problems with stochastic parameters: Application to heat conduction with variable Robin coefficient, *Computer Methods in Applied Mechanics and Engineering* 198 (41-44) (2009) 3187–3206. doi:10.1016/j.cma.2009.05.019.
URL <http://linkinghub.elsevier.com/retrieve/pii/S0045782509002114>
- [51] F. Vidal-Codina, N. C. Nguyen, M. B. Giles, J. Peraire, An empirical interpolation and model-variance reduction method for computing statistical outputs of parametrized stochastic partial differential equations, *SIAM-ASA Journal on Uncertainty Quantification* 4 (1) (2016) 244–265. doi:10.1137/15M1016783.
- [52] C. W. Rowley, I. G. Kevrekidis, J. E. Marsden, K. Lust, Reduction and reconstruction for self-similar dynamical systems, *Nonlinearity* 16 (4) (2003) 1257–1275. doi:10.1088/0951-7715/16/4/304.
- [53] A. Iollo, D. Lombardi, Advection modes by optimal mass transfer, *Physical Review E - Statistical, Nonlinear, and Soft Matter Physics* 89 (2) (2014). doi:10.1103/PhysRevE.89.022923.

- [54] R. L. Van Heyningen, N. C. Nguyen, P. Blonigan, J. Peraire, Adaptive Model Reduction of High-Order Solutions of Compressible Flows via Optimal Transport, *International Journal of Computational Fluid Dynamics* 37 (6) (2023) 541–563. doi:10.1080/10618562.2024.2326559.
- [55] N. C. Nguyen, R. L. Van Heyningen, J. Vila-Pérez, J. Peraire, Optimal transport for mesh adaptivity and shock capturing of compressible flows (2024). arXiv:2310.01196, doi:10.1016/j.jcp.2024.113005.
- [56] N. C. Nguyen, Model reduction techniques for parametrized nonlinear partial differential equations, in: *Advances in Applied Mechanics*, Vol. 58, Elsevier, 2024, pp. 135–190. doi:10.1016/bs.aams.2024.03.005.
URL <https://www.sciencedirect.com/science/article/pii/S0065215624000073>
- [57] N. C. Nguyen, J. Peraire, Hybridizable Discontinuous Galerkin Methods for the Two-Dimensional Monge–Ampère Equation, *Journal of Scientific Computing* 100 (2) (2024) 44. doi:10.1007/s10915-024-02604-3.
URL <https://doi.org/10.1007/s10915-024-02604-3>
- [58] J. Reiss, P. Schulze, J. Sesterhenn, V. Mehrmann, The shifted proper orthogonal decomposition: A mode decomposition for multiple transport phenomena, *SIAM Journal on Scientific Computing* 40 (3) (2018) A1322–A1344. arXiv:1512.01985, doi:10.1137/17M1140571.
- [59] D. Rim, S. Moe, R. J. LeVeque, Transport reversal for model reduction of hyperbolic partial differential equations, *SIAM-ASA Journal on Uncertainty Quantification* 6 (1) (2018) 118–150. arXiv:1701.07529, doi:10.1137/17M1113679.
- [60] N. J. Nair, M. Balajewicz, Transported snapshot model order reduction approach for parametric, steady-state fluid flows containing parameter-dependent shocks, *International Journal for Numerical Methods in Engineering* 117 (12) (2019) 1234–1262. arXiv:1712.09144, doi:10.1002/nme.5998.
- [61] T. Taddei, A registration method for model order reduction: Data compression and geometry reduction, *SIAM Journal on Scientific Computing* 42 (2) (2020) A997–A1027. arXiv:1906.11008, doi:10.1137/19M1271270.

- [62] M. J. Zahr, P. O. Persson, An optimization-based approach for high-order accurate discretization of conservation laws with discontinuous solutions, *Journal of Computational Physics* 365 (2018) 105–134. [arXiv:1712.03445](#), [doi:10.1016/j.jcp.2018.03.029](#).
- [63] M. J. Zahr, A. Shi, P. O. Persson, Implicit shock tracking using an optimization-based high-order discontinuous Galerkin method, *Journal of Computational Physics* 410 (2020) 109385. [arXiv:1912.11207](#), [doi:10.1016/j.jcp.2020.109385](#).
- [64] J. B. Rutzmoser, D. J. Rixen, P. Tiso, S. Jain, Generalization of quadratic manifolds for reduced order modeling of nonlinear structural dynamics, *Computers and Structures* 192 (2017) 196–209. [arXiv:1610.09906](#), [doi:10.1016/j.compstruc.2017.06.003](#).
- [65] K. Lee, K. T. Carlberg, Model reduction of dynamical systems on nonlinear manifolds using deep convolutional autoencoders, *Journal of Computational Physics* 404 (2020) 108973. [arXiv:1812.08373](#), [doi:10.1016/j.jcp.2019.108973](#).
- [66] R. Geelen, S. Wright, K. Willcox, Operator inference for non-intrusive model reduction with quadratic manifolds, *Computer Methods in Applied Mechanics and Engineering* 403 (2023) 115717. [arXiv:2205.02304](#), [doi:10.1016/j.cma.2022.115717](#).
- [67] J. Barnett, C. Farhat, Quadratic approximation manifold for mitigating the Kolmogorov barrier in nonlinear projection-based model order reduction, *Journal of Computational Physics* 464 (2022). [arXiv:2204.02462](#), [doi:10.1016/j.jcp.2022.111348](#).
- [68] B. Kramer, K. E. Willcox, Nonlinear model order reduction via lifting transformations and proper orthogonal decomposition, *AIAA Journal* 57 (6) (2019) 2297–2307. [arXiv:1808.02086](#), [doi:10.2514/1.J057791](#).
- [69] E. Qian, B. Kramer, B. Peherstorfer, K. Willcox, Lift & Learn: Physics-informed machine learning for large-scale nonlinear dynamical systems, *Physica D: Nonlinear Phenomena* 406 (2020). [arXiv:1912.08177](#), [doi:10.1016/j.physd.2020.132401](#).
- [70] S. A. McQuarrie, P. Khodabakhshi, K. E. Willcox, Nonintrusive Reduced-Order Models for Parametric Partial Differential Equations via

- Data-Driven Operator Inference, *SIAM Journal on Scientific Computing* 45 (4) (2023) A1917–A1946. doi:10.1137/21M1452810.
URL <https://doi.org/10.1137/21M1452810>
- [71] B. Kramer, B. Peherstorfer, K. E. Willcox, Learning Nonlinear Reduced Models from Data with Operator Inference (2024). doi:10.1146/annurev-fluid-121021-025220.
- [72] M. Barrault, Y. Maday, N. C. Nguyen, A. T. Patera, An 'empirical interpolation' method: application to efficient reduced-basis discretization of partial differential equations, *Comptes Rendus Mathematique* 339 (9) (2004) 667–672. doi:10.1016/J.Crma.2004.08.006.
URL <http://www.sciencedirect.com/science/article/pii/S1631073X04004248><http://linkinghub.elsevier.com/retrieve/pii/S1631073X04004248>
- [73] M. A. Grepl, Y. Maday, N. C. Nguyen, A. T. Patera, Efficient reduced-basis treatment of nonaffine and nonlinear partial differential equations, *Mathematical Modelling and Numerical Analysis* 41 (3) (2007) 575–605. doi:10.1051/m2an:2007031.
URL <http://www.esaim-m2an.org/10.1051/m2an:2007031>http://journals.cambridge.org/abstract/_jS0764583X07000313
- [74] D. Galbally, K. Fidkowski, K. Willcox, O. Ghattas, Non-linear model reduction for uncertainty quantification in large-scale inverse problems, *International Journal for Numerical Methods in Engineering* 81 (12) (2010) 1581–1608. doi:10.1002/nme.2746.
- [75] J. L. Eftang, M. A. Grepl, A. T. Patera, A posteriori error bounds for the empirical interpolation method, *Comptes Rendus Mathematique* 348 (9–10) (2010) 575–579. doi:10.1016/j.crma.2010.03.004.
- [76] M. Drogmann, B. Haasdonk, M. Ohlberger, Reduced basis approximation for nonlinear parametrized evolution equations based on empirical operator interpolation, *SIAM Journal on Scientific Computing* 34 (2) (2012) A937–A969. doi:10.1137/10081157X.
- [77] A. Manzoni, A. Quarteroni, G. Rozza, Shape optimization for viscous flows by reduced basis methods and free-form deformation, *International*

- Journal for Numerical Methods in Fluids 70 (5) (2012) 646–670. doi:10.1002/flid.2712.
- [78] J. S. Hesthaven, C. Pagliantini, G. Rozza, Reduced basis methods for time-dependent problems, *Acta Numerica* 31 (2022) 265–345. doi:10.1017/S0962492922000058.
- [79] Y. Chen, S. Gottlieb, L. Ji, Y. Maday, An EIM-degradation free reduced basis method via over collocation and residual hyper reduction-based error estimation, *Journal of Computational Physics* 444 (2021) 110545. doi:10.1016/j.jcp.2021.110545.
- [80] N. C. Nguyen, J. Peraire, N. C. Nguyen, J. Peraire, An efficient reduced-order modeling approach for non-linear parametrized partial differential equations, *International Journal for Numerical Methods in Engineering* 76 (1) (2008) 27–55. doi:10.1002/nme.2309. URL <http://doi.wiley.com/10.1002/nme.2309>
- [81] Y. Maday, O. Mula, A. T. Patera, M. Yano, The Generalized Empirical Interpolation Method: Stability theory on Hilbert spaces with an application to the Stokes equation, *Computer Methods in Applied Mechanics and Engineering* 287 (2015) 310–334. doi:10.1016/j.cma.2015.01.018.
- [82] Y. Maday, O. Mula, A generalized empirical interpolation method: Application of reduced basis techniques to data assimilation, in: *Springer INdAM Series*, Vol. 4, Springer, 2013, pp. 221–235. arXiv:1512.00683, doi:10.1007/978-88-470-2592-9-13.
- [83] N. C. Nguyen, J. Peraire, Efficient and accurate nonlinear model reduction via first-order empirical interpolation, *Journal of Computational Physics* 494 (2023) 112512. arXiv:2305.00466, doi:10.1016/j.jcp.2023.112512. URL <http://arxiv.org/abs/2305.00466>
- [84] N. C. Nguyen, First-order empirical interpolation method for real-time solution of parametric time-dependent nonlinear PDEs (2024). arXiv:2410.02093. URL <https://arxiv.org/abs/2410.02093>

- [85] N. C. Nguyen, High-order empirical interpolation methods for real time solution of parametrized nonlinear PDEs (2024). arXiv:2410.02100. URL <https://arxiv.org/abs/2410.02100>
- [86] N. C. Nguyen, A. Rohskopf, Proper Orthogonal Descriptors for Efficient and Accurate Interatomic Potentials, Journal of Computational Physics 480 (2022) 112030. arXiv:2209.02362, doi:<https://doi.org/10.1016/j.jcp.2023.112030>. URL <http://arxiv.org/abs/2209.02362><https://www.sciencedirect.com/science/article/pii/S0021999123001250>
- [87] N. C. Nguyen, Fast proper orthogonal descriptors for many-body interatomic potentials, Physical Review B 107 (14) (2023) 144103. arXiv:2212.14446, doi:[10.1103/PhysRevB.107.144103](https://doi.org/10.1103/PhysRevB.107.144103). URL <http://arxiv.org/abs/2212.14446>
- [88] N. C. Nguyen, Proper orthogonal descriptors for multi-element chemical systems, Journal of Computational Physics 511 (2024) 113102. arXiv:2212.14549, doi:[10.1016/j.jcp.2024.113102](https://doi.org/10.1016/j.jcp.2024.113102). URL <https://www.sciencedirect.com/science/article/pii/S0021999124003516>
- [89] N. C. Nguyen, D. Sema, Environment-adaptive machine learning potentials, Phys. Rev. B 110 (6) (2024) 64101. doi:[10.1103/PhysRevB.110.064101](https://doi.org/10.1103/PhysRevB.110.064101). URL <https://link.aps.org/doi/10.1103/PhysRevB.110.064101>